Quantum-dot all-optical logic in a structured vacuum

Xun Ma and Sajeev John
Department of Physics, University of Toronto, Toronto, Canada M5S 1A7
(Received 27 April 2011; published 27 July 2011)

We demonstrate multiwavelength channel optical logic operations on the Bloch vector of a quantum two-level system in the structured electromagnetic vacuum of a bimodal photonic crystal waveguide. This arises through a bichromatic strong-coupling effect that enables unprecedented control over single quantum-dot (QD) excitation through two beams of ultrashort femtojoule pulses. The second driving pulse (signal) with slightly different frequency and weaker strength than the first (holding) pulse leads to controllable strong modulation of the QD Bloch vector evolution path. This occurs through resonant coupling of the signal pulse with the Mollow sideband transitions created by the holding pulse. The movement of the Mollow sidebands during the passage of the holding pulse leads to an effective chirping in transition frequency seen by the signal. Bloch vector dynamics in the rotating frame of the signal pulse and within the dressed-state basis created by the holding pulse reveals that this chirped coupling between the signal pulse and the Mollow sidebands leads to either augmentation or negation of the final quantum-dot population (after pulse passage) compared to the outcome of the holding pulse alone and depending on the relative frequencies of the pulses. By making use of this extra degree of freedom for ultrafast control of QD excitations, applications in ultrafast all-optical logic AND, OR, and NOT gates are proposed in the presence of significant (0.1) THz nonradiative dephasing and (about 1%) inhomogeneous broadening.

DOI: 10.1103/PhysRevA.84.013830 PACS number(s): 42.50.Hz, 42.70.Qs, 32.80.−t, 42.50.Ct

I. INTRODUCTION

Photonic band-gap (PBG) materials are a special class of photonic crystals (PC's) that facilitate light localization [1,2] and control of spontaneous emission [3,4] from atoms. They offer unprecedented engineering capabilities to design electromagnetic (EM) dispersion relations, thereby changing the vacuum EM density of states (DOS) over extended spectral ranges. The EM DOS structure in photonic crystals provides an ideal environment for exploring quantum optical phenomena [4–11] with important consequences for microphotonic device development. The performance of PC-based devices can be significantly better than their conventional counterparts due to the strong confinement of light within an optical microchip. The small PC defect mode volume leads to extremely strong optical fields at very low power levels for exceptional nonlinear optical effects. Moreover, PBG waveguides enable subwavelength scale circuits for diffractionless guidance of light on a chip in three dimensions [12–16]. As a result, PBG materials represent a broad and robust platform for integrated photonics.

Many new quantum optical phenomena are predicted to occur within the unusual vacuum DOS structure of photonic crystals. The strong suppression of DOS for frequencies within the PBG leads to increased spontaneous emission lifetime [4], photon-atom bound states [5], and localization of superradiance [6]. Whereas the PBG is often regarded as a spectral range with vanishing electromagnetic DOS, engineered defects in the otherwise periodic microstructure can create greatly enhanced local density of states (LDOS) and field enhancement in small mode volumes [17–19]. This enhanced coherent coupling to light emitters can be combined with suppressed background incoherent coupling deep inside the PBG. Experimental realization of single quantum-dot (QD) strong coupling inside a PC cavity [18] and other types of cavities [20–24] have been reported. This has sparked broad interest in on-chip quantum electrodynamics.

The electromagnetic vacuum influences light-matter interactions through radiative relaxation of the atomic dipole and population. This relaxation has traditionally been considered incompatible with strong-coupling effects. Therefore, most strong-coupling studies have focused on minimizing dissipation to EM continuum modes. However, it has been recently shown that discontinuous LDOS inside photonic crystals can bring novel dynamics into strong-coupling phenomena, especially when the length-of-interaction time scale Δ_t (e.g., pulse duration, observation time, etc.) is comparable to or much longer than the relaxation time scale $1/\Gamma$. For example, in the steady-state time regime where $\Delta_t \gg 1/\Gamma$, a discontinuous jump from low to high LDOS at cutoff in a bimodal waveguide enables switching of the two-level quantum-dot population from below to above inversion at a continuous wave (cw) driving laser field threshold [7–9]. This is due to the imbalance of radiative emission rates among the laser-induced Mollow sidebands that straddle the LDOS discontinuity.

The steady-state population switching turns into a more dramatic dynamic population switching [10,11] for a coherent optical pulse with duration comparable with radiative relaxation rates ($\Delta_t \sim 1/\Gamma$). Near the LDOS discontinuity, radiative relaxation rates of the driven QD become highly field dependent. This is accompanied by a "vacuum structure term" in the atomic Bloch equations. Suppose the QD transition (in the absence of an external field) lies in the low LDOS region with a single waveguide mode. Under strong driving field, the QD will experience enhanced coupling to the slow group velocity states of the second mode of the waveguide that exhibits a cutoff. One of the QD Mollow sidebands then experiences a high LDOS with accelerated radiative relaxation. Under weak field, the QD will be decoupled from the high LDOS, with decreased radiative relaxation. This makes it possible to control radiative relaxation time scale through field strength and dynamically change the interaction regime (from coherent transient to field-enhanced decay, and vice versa)

within a single-pulse duration. In this mixed interaction time scenario, a single control laser pulse is capable of high-contrast dynamical switching of QD populations on a picosecond time scale with femtojoule energy levels. Population inversion is activated and deactivated by picosecond pulse trains detuned below and above the atomic resonance, respectively. This dynamic inversion is due to the rapid rise in relaxation rates as the pulse amplitude rises, causing the Bloch vector to switch from antiparallel to parallel alignment with the pulse torque vector into a slightly inverted state (steady-state attraction process). Subsequent near-complete inversion occurs through a coherent adiabatic following process as the pulse amplitude subsides. The system reverts to slow relaxation and the QD remains inverted long after the pulse has departed. This single-pulse dynamic switching is a strong-coupling effect that results from the interplay between coherent transient dynamics and field-dependent radiative relaxation inside discontinuous LDOS vacuum structures (structured vacua).

In this paper, we develop a general framework which encompasses both the steady-state switching [7–9] and single-pulse dynamic switching effects [10,11], and allows us to introduce an additional driving pulse (signal pulse) to modulate the evolution of a QD, already dressed by a strong holding laser pulse in a PBG waveguide. The weaker modulating signal pulse is treated as a perturbation to the dressed levels of the QD created by the holding pulse. Nevertheless, the signal pulse introduces rich modulation effects in the final QD inversion when its frequency coincides with one of the QD Mollow sidebands induced by the holding pulse. The secondary signal pulse is designed to probe the moving Mollow sidebands caused by transitions among dressed levels of the QD, which depends on the holding-pulse amplitude. As the holding-pulse amplitude varies, the detuning between the Mollow sidebands and the signal-pulse frequency is effectively chirped. As a result of this chirping, after the Bloch vector is attracted to the steady state at the peak of the two pulses (same as in the single-pulse dynamic switching effect), it then adiabatically follows the chirped movement of the signal-pulse torque vector, bringing the QD to the opposite inversion state as compared to the nonchirped single-pulse dynamic switching. More specifically, while a single negatively detuned holding pulse (redshifted) inverts the quantum dot after passage, the simultaneous presence of a properly detuned signal pulse modulates the population to below inversion after passage. On the other hand, while a single positively detuned holding pulse (blueshifted) de-excites the quantum dot, simultaneously sending in a properly detuned signal pulse leads to final population inversion. The bichromatically driven QD system offers a new degree of freedom to logically control QD excitation states, not available in single-pulse dynamic switching.

The required electromagnetic vacuum structure with discontinuous LDOS can be realized through engineered defects inside otherwise periodic photonic crystals. For example, waveguide architectures within a three-dimensional (3D) PBG provide very large LDOS jumps via mode cutoff. In the high LDOS region, Purcell factors (ratio of spontaneous emission rate to that in free space) of several thousand are possible in waveguide segments less than 20 unit cells [25,26]. This accelerates spontaneous emission to occur in a picosecond, superceding phonon-mediated (nonradiative) relaxation even at moderate temperatures. This ultrafast radiative relaxation enables single-pulse dynamic switching in picosecond all-optical switches [10,11]. With the extra flexibility in QD control provided by the secondary signal pulse, we demonstrate the full range of ultrafast all-optical AND, OR, and NOT logic operations.

In Sec. II, we establish the theoretical framework for describing the evolution of a QD Bloch vector driven by two external pulses within the discontinuous LDOS vacuum structure. In Sec. III, we give a detailed exposition of the bichromatic QD inversion modulation effect through the effective chirping between signal-pulse and holding-pulse dressed transitions. In Sec. IV, we discuss possible applications to ultrafast all-optical AND, OR, and NOT gates, including inhomogeneous QD line broadening and nonradiative dephasing. In Sec. V, we compare our bichromatic control mechanism with other widely applied coherent adiabatic inversion techniques. We also present our conclusions and discuss future directions.

II. EQUATION OF MOTION FOR THE DRIVEN QUANTUM DOT

We consider a two-level system (e.g., quantum dot) with transition frequency ω_A detuned slightly from a step discontinuity in the electromagnetic density of states at frequency ω_E. A strong holding laser pulse $E_h(t)$ and a weaker signal pulse $E_s(t)$ [with central frequencies $\omega_{h,s}$ and envelope functions $\mathcal{E}_{h,s}(t)$] interact simultaneously with this QD. The step-shaped electromagnetic DOS can be provided by a waveguide cutoff mode within a 3D-2D PBG heterostructure as discussed in previous work [10,11]. In addition, the two-level system interacts with a smooth featureless nonradiative reservoir that is statistically independent from the photonic reservoir. This coupling to phonons causes dephasing of the atomic dipole. The contributions of the two reservoirs to the evolution of the reduced density operator of the two-level system are assumed to factorize so as to be treated separately.

We consider classical control and signal pulses with electric field

$$E_{h,s}(t) = \mathcal{E}_{h,s}(t)\cos(\omega_{h,s}t + \phi_{h,s}). \tag{1}$$

The Hamiltonian, in the absence of phonon coupling, consists of three parts:

$$H = H_S + H_R + H_{SR}, \tag{2}$$

where H_S is the Hamiltonian of the pulse-driven atom, H_R describes the electromagnetic reservoir, and H_{SR} is the atom-reservoir coupling. In the bare atomic basis (ground state $|1\rangle$ and excited state $|2\rangle$), this Hamiltonian [in the rotating-wave approximation (RWA) in rotating frame ω_h] takes the form

$$\begin{aligned} H_S &= \frac{1}{2}\hbar\Delta_{Ah}\sigma_3 - \hbar[\epsilon_h + \epsilon_s e^{-i(\delta_s t+\phi_s)}]\sigma_{21} \\ &\quad - \hbar[\epsilon_h + \epsilon_s e^{i(\delta_s t+\phi_s)}]\sigma_{12}, \\ H_R &= \sum_\lambda \hbar\omega_\lambda a_\lambda^\dagger a_\lambda, \\ H_{SR} &= i\hbar\sum_\lambda g_\lambda(a_\lambda^\dagger\sigma_{12} - a_\lambda\sigma_{21}). \end{aligned} \tag{3}$$

Here, the time-dependent Rabi frequency $\epsilon_{h,s}(t) = d_{21}|\mathcal{E}_{h,s}(t)|/\hbar$, and $\mathbf{d_{21}}$ is the quantum-dot dipole transition matrix element. We assume $|\mathbf{d_{12}}| = |\mathbf{d_{21}}| = d_{21}$, $\mathcal{E}_{h,s}(t) = \mathcal{E}_{h,s}(t)^*$, and that the dipole is parallel to the pulse polarization for simplicity. $a_\lambda^\dagger$ and a_λ are the creation and annihilation operators of mode λ of the electromagnetic reservoir with frequency ω_λ. We define the bare atomic operators $\sigma_{ij} = |i\rangle\langle j|(i,j = 1,2)$, population inversion $\sigma_3 = \sigma_{22} - \sigma_{11}$, the detunings $\Delta_{Ah} = \omega_A - \omega_h$, $\Delta_\lambda = \omega_\lambda - \omega_h$, $\delta_s = \omega_s - \omega_h$, and we choose $\phi_h = 0$.

A. Dressed states

The coupling of the two-level quantum dot to the two driving pulses results in a set of energy eigenstates, the doubly dressed states, composed of an infinite number of manifolds, each containing an infinite number of energy levels. The fluorescence spectrum as a result of spontaneous emissions among selected levels of the doubly dressed states depends on the relative strength and detuning of the two driving beams and exhibits distinct features from the Mollow triplet of single dressed states. As shown in Fig. 1 (from [27]), when ϵ_s is much smaller than ϵ_h, the fluorescence peaks are confined in three regions ω_h and $\omega_h \pm 2\Omega_h$ (each composed of triplets or doublets depending on signal-holding beam detuning) that can be viewed as evolved from the single-beam Mollow triplet. However, as ϵ_s increases, not only do the splittings within each doublet or triplet increase, but there are also additional high-order multiple peaks emerging at $\omega_s \pm 4\Omega_h$, $\omega_s \pm 6\Omega_h$, etc.

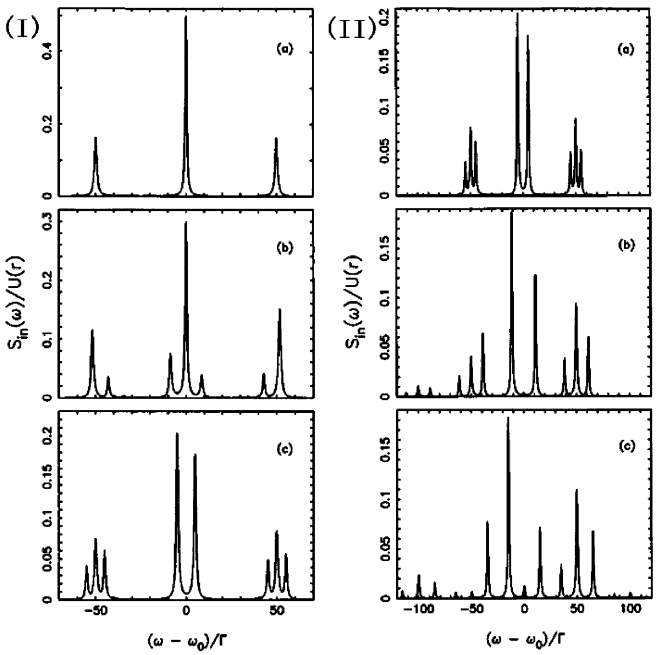

FIG. 1. (From [27]) Fluorescence spectrum of two-level atom in ordinary vacuum (with radiative decay rate Γ) driven by a bichromatic field with one strong (holding) and one weak (signal) component. (I) Fluorescence spectrum for $\omega_h = \omega_A$, $2\epsilon_h = 50\Gamma$, $\epsilon_s/\epsilon_h = 0.2$, and different detunings $\Delta_{+s} = (\omega_h + 2\Omega_h) - \omega_s$ between the signal beam and the right Mollow sideband of the holding beam (Ω_h being the generalized Rabi frequency of the holding beam): [I(a)] $\Delta_{+s} \ll 50\Gamma$; [I(b)] $\Delta_{+s} = 7\Gamma$; [I(c)] $\Delta_{+s} = 0$. (II) Fluorescence spectrum for $\omega_h = \omega_A$, $2\epsilon_h = 50\Gamma$, $\Delta_{+s} = 0$, and different Rabi frequency ratio: [II(a)] $\epsilon_s/\epsilon_h = 0.2$; [II(b)] $\epsilon_s/\epsilon_h = 0.4$; [II(c)] $\epsilon_s/\epsilon_h = 0.6$.

As the fluorescence spectrum becomes more complex and its overall range widens with increasing signal field, a general derivation of the master equation for bichromatically driven quantum dots in the structured vacuum is difficult. To simplify the model, we assume that the signal field is much weaker than the holding field $\epsilon_s \ll \epsilon_h$, so that the fluorescence spectrum is confined in the three regions ω_h and $\omega_h \pm 2\Omega_h$ of the central, left, and right Mollow sidebands of the holding pulse. In this situation, instead of working in the complex doubly driven dressed-state basis, we work in the dressed-state basis of the holding pulse and treat the signal field as a perturbative time-dependent modulation on this singly driven dressed state. This assumption leads to the following time-dependent dressed states $|\tilde{1}\rangle$ and $|\tilde{2}\rangle$ that diagnolizes H_S:

$$\begin{aligned} |\tilde{1}\rangle &= c(t)|1\rangle + s(t)|2\rangle, \\ |\tilde{2}\rangle &= -s(t)|1\rangle + c(t)|2\rangle, \end{aligned} \tag{4}$$

where

$$\begin{aligned} c^2(t) &= \{1 + \Delta_{AL}/[2\Omega(t)]\}/2, \\ s^2(t) &= \{1 - \Delta_{AL}/[2\Omega(t)]\}/2, \\ \Omega(t) &= [(\Delta_{AL}/2)^2 + |\epsilon_h + \epsilon_s e^{-i(\delta_s t+\phi_s)}|^2]^{1/2}. \end{aligned} \tag{5}$$

The dressed-state atomic operators are defined similarly as their bare-state counterparts:

$$\begin{aligned} \tilde{R}_{ij} &= |\tilde{i}\rangle\langle\tilde{j}|(i,j = 1,2), \\ \tilde{R}_3 &= \tilde{R}_{22} - \tilde{R}_{11}. \end{aligned}$$

B. Master equation

By working in the dressed-state basis, Eq. (4), the master equation that governs the temporal evolution of the reduced quantum-dot density operator can be derived. The details are shown in Appendices A and B. This master equation, when represented in the bare atomic basis $|1\rangle$ and $|2\rangle$, has the following form:

$$\begin{aligned} \dot{\varrho} = &-i\Omega R_3\varrho - \frac{\gamma_0 c^2 s^2 + \gamma_p (c^2 - s^2)^2}{2}(\varrho - R_3\varrho R_3) \\ &- \frac{\gamma_+ c^4 + 4\gamma_p c^2 s^2}{2}(R_{22}\varrho - R_{12}\varrho R_{21}) \\ &- \frac{\gamma_- s^4 + 4\gamma_p c^2 s^2}{2}(R_{11}\varrho - R_{21}\varrho R_{12}) \\ &- \frac{cs}{2}[s^2\gamma_0(R_{12}\varrho - R_3\varrho R_{12}) + c^2\gamma_+(R_{12}\varrho + R_{12}\varrho R_3) \\ &+ s^2\gamma_-(\varrho R_{12} - R_3\varrho R_{12}) + c^2\gamma_0(\varrho R_{12} + R_{12}\varrho R_3)] \\ &- \frac{c^2 s^2}{2}(\gamma_- + \gamma_+)R_{21}\varrho R_{21} + \text{H.c.} \end{aligned} \tag{6}$$

Here, $\gamma_{0,\pm}$ are the radiative decay rates at the central, right, and left Mollow sidebands dressed by the holding pulse alone (details in Appendices A and B). γ_p is the phonon dephasing rate.

This master equation is derived in the signal-pulse-modulated dressed-state basis of the holding-pulse

equation (4), and is valid when signal pulse is small compared with holding pulse so that the spectrum of the dressed system is confined in the neighborhood of the holding-pulse Mollow triplet [Fig. 1, II(a)]. If the signal pulse is strong enough to induce higher-order harmonics [Fig. 1, II(c)], these higher-order resonances (across a wide spectrum) will need to enter the master equation, each of them sensing a distinct DOS in the structured vacuum of the photonic crystal waveguide. In this situation, Eq. (6) will no longer be sufficient to describe the dressed system dynamics in the structured vacuum.

C. Optical Bloch equation

Using the master equation (6), the temporal evolution of the quantum-dot reduced density operator is known. The Bloch equation that governs the evolution of the quantum-dot population and polarization is then obtained by taking the expectation values of the atomic operators with respect to the reduced density operator.

We define the in-phase and in-quadrature parts of the atomic dipole operators as

$$\begin{aligned} \sigma_1 &= \sigma_{12} + \sigma_{21}, \\ \sigma_2 &= i(\sigma_{12} - \sigma_{21}). \end{aligned} \tag{7}$$

By using Eq. (6) and setting $\gamma_0 = \gamma_+$ for our LDOS model, the following Bloch component equations are obtained (same derivation as the Bloch equation for a QD driven by a single pulse [11]):

$$\begin{aligned} \langle\dot{\sigma_1}\rangle &= -\Delta_{AL}\langle\sigma_2\rangle - 2\epsilon_s \sin\phi\langle\sigma_3\rangle - \frac{1}{T_u}\langle\sigma_1\rangle + V, \\ \langle\dot{\sigma_2}\rangle &= \Delta_{AL}\langle\sigma_1\rangle + 2(\epsilon_h + \epsilon_s\cos\phi)\langle\sigma_3\rangle - \frac{1}{T_v}\langle\sigma_2\rangle, \\ \langle\dot{\sigma_3}\rangle &= -2(\epsilon_h + \epsilon_s\cos\phi)\langle\sigma_2\rangle + 2\epsilon_s\sin\phi\langle\sigma_1\rangle \\ &\quad -\frac{1}{T_w}(\langle\sigma_3\rangle + 1) + V\langle\sigma_1\rangle. \end{aligned} \tag{8}$$

Here, $\phi(t) = \delta_s t + \phi_s$, $1/T_{u,v} = \Gamma_{u,v} = \frac{c^2(1+s^2)\gamma_+ + s^4\gamma_- + 4\gamma_p}{2} \mp \frac{c^2 s^2(\gamma_+ - \gamma_-)}{2}$, $1/T_w = \Gamma_w = c^2(1+s^2)\gamma_+ + s^4\gamma_-$ and $V = (\gamma_+ - \gamma_-)cs^3$. T_u and T_v reduce to the transverse dephasing time, and T_w reduces to the longitudinal dephasing time in ordinary vacuum if we set $\gamma_+ = \gamma_-$. The Bloch component equations can be written in vector form

$$\dot{\boldsymbol{\rho}} = \Omega \times \boldsymbol{\rho} - \Gamma_{\boldsymbol{\rho}} + \mathbf{C}, \tag{9}$$

where

$$\begin{aligned} \boldsymbol{\rho} &= (\langle\sigma_1\rangle, \langle\sigma_2\rangle, \langle\sigma_3\rangle) = (u, v, w), \\ \Omega = \Omega_h + \Omega_s &= (-2\epsilon, 0, \Delta_{AL}) + (-2\epsilon_s\cos\phi, -2\epsilon_s\sin\phi, 0), \\ \Gamma_{\boldsymbol{\rho}} &= (u/T_u, v/T_v, w/T_w), \\ \mathbf{C} &= (V, 0, -1/T_w + Vu). \end{aligned}$$

The incoherent terms in Eq. (9) are similar to that of a QD driven by the holding pulse alone [10,11], except that the dressed-state coefficients c and s now contain oscillating components coming from the detuning frequency δ_s of the signal pulse from the holding pulse. As with the master equation (6), the Bloch equation (9) is valid when the signal pulse is weak compared with the holding pulse so that it can be considered as a perturbative modulation to the singly dressed Q-dot states due to the holding pulse alone, and the fluorescence spectrum of the quantum dot is confined in the three regions around the Mollow triplet of the holding pulse (Fig. 1). As with the singly driven quantum dot [10,11], the "vacuum structure term" V and strongly field-dependent relaxation rates $1/T_{u,v,w}$ significantly alter the temporal evolution of the atomic Bloch vector as the quantum dot interacts with the optical pulses. Both of these features are absent in a conventional (unstructured) electromagnetic vacuum. More specifically, the relaxation rates are enhanced under strong field and suppressed in weak field. As a result, the Bloch vector experiences fast relaxation toward the steady state near the peak of the pulse (steady-state attraction process [10,11]), but reverts to coherent evolution as the pulse subsides.

A significant difference between the doubly driven system and a singly driven system arises from the coherent driving terms (Fig. 2). In addition to the holding-pulse torque vector $\boldsymbol{\Omega}_h$ that moves in the u-w plane at a rate of order τ^{-1} (τ being the pulse duration), the torque vector $\boldsymbol{\Omega}_s$ of the signal pulse oscillates in the u-v plane at the beating frequency δ_s between the two pulses. This signal torque vector provides an additional control degree of freedom of the quantum dot. We denote the angle between $\boldsymbol{\Omega}_h$ and the w axis as α, the angle between $\boldsymbol{\Omega}_s$ and the negative u axis direction as ϕ, and the angle between the total torque vector $\boldsymbol{\Omega} = \boldsymbol{\Omega}_h + \boldsymbol{\Omega}_s$ and the w axis as θ. The precession of the Bloch vector around $\boldsymbol{\Omega}$ determines the coherent evolution of the Q dot. As we show later, the steady-state attraction near the peak of the pulse, combined with the bichromatic coherent evolution as the pulses subside, enables ultrafast all-optical logic operations in the PBG microchip.

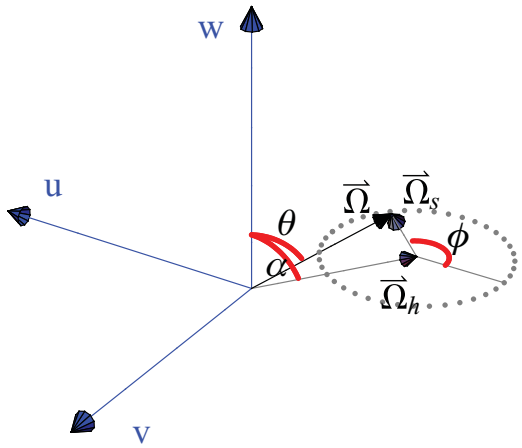

FIG. 2. (Color online) Torque vectors of the holding and signal pulses. The holding-pulse torque vector $\boldsymbol{\Omega}_h$ moves in the u-w plane at a rate of order τ^{-1} (τ being the pulse duration), while the signal-pulse torque vector $\boldsymbol{\Omega}_s$ oscillates in the u-v plane at the beating frequency δ_s between the two pulses. We denote the angle between $\boldsymbol{\Omega}_h$ and the w axis as α, the angle between $\boldsymbol{\Omega}_s$ and the negative u axis direction as ϕ, and the angle between the total torque vector $\boldsymbol{\Omega} = \boldsymbol{\Omega}_h + \boldsymbol{\Omega}_s$ and the w axis as θ. The precession of the Bloch vector around $\boldsymbol{\Omega}$ determines the coherent evolution of the Q dot.

III. BICHROMATIC QUANTUM-DOT INVERSION MODULATION

For a single continuous wave holding beam, the steady state of Eq. (9) can be solved analytically to reveal the single-beam steady-state switching effect [7–9]. If both the holding and signal beams are continuous, the steady state of the Bloch equation can be solved semianalytically through Floquet expansion at the beating frequency δ_s [28]. Similar steady-state switching effects can be obtained in this multiple cw beam system, with the susceptibility spectrum composed of multiple peaks near each of the Mollow sidebands instead of a single Mollow peak.

When the driving beams are short pulses, the steady-state solution is insufficient to describe the Bloch vector evolution. Numerical solution of Eq. (9) reveals a strong-coupling effect in this structured vacuum involving fast attraction to the steady state at the pulse peak followed by various coherent evolution processes near the pulse tail when radiative relaxation is slower. As shown previously, when a single strong pulse interacts with the quantum dot ($\epsilon_s = 0$), dynamic population inversion switching is obtained by a combination of the steady-state attraction and coherent adiabatic following [10,11]. A single redshifted holding pulse ($\Delta_{Ah} > 0$) inverts the quantum dot after passage [Fig. 3(a), dashed line], while a single blueshifted pulse ($\Delta_{Ah} < 0$) de-excites the quantum dot after passage [Fig. 3(b), dashed line]. This dynamic population switching mechanism has been suggested for ultrafast all-optical switching at very low power levels [10,11].

Further control of the quantum-dot population is possible by sending an additional signal pulse ϵ_s to interact simultaneously with the quantum dot. As shown in Fig. 3(a), while a single negatively detuned holding pulse ($\Delta_{Ah} > 0$) inverts the quantum dot after passage (dashed curve), the coincident traversal of a properly detuned signal pulse negates the population inversion after passage. On the other hand, as shown in Fig. 3(b), while a single positively detuned holding pulse ($\Delta_{Ah} < 0$) de-excites the quantum dot from an arbitrary initial state to ground state (dashed curve), a properly detuned and simultaneous signal pulse ϵ_s is able to reinvert the final population (solid curve).

The amplitude of population modulation by a secondary signal pulse depends sensitively on various factors. Figure 4 shows the final population reached after the passage of the pulses as a function of detuning δ_s. Again, when only the holding pulse is present ($\epsilon_s = 0$, thick dotted-dashed lines), the quantum dot reaches positive inversion when $\Delta_{Ah} > 0$ [Fig. 4(a)] and negative inversion when $\Delta_{Ah} < 0$ [Fig. 4(b)]. The simultaneous presence of the signal pulse induces complex modulations of the final inversion that depend strongly on δ_s (solid and dashed curves). If we denote $|\mathbf{\Omega}_h^{\min}| = |\Delta_{Ah}|$ and $|\mathbf{\Omega}_h^{\max}| = \sqrt{\Delta_{Ah}^2 + (2\epsilon_h^{\max})^2}$ as the minimum and maximum Mollow splitting generated by the holding pulse alone during its passage ($\epsilon_h^{\max}$ being the peak Rabi frequency of the holding pulse), then the largest inversion modulation appears when the signal frequency ω_s falls in the region $(\omega_h + |\mathbf{\Omega}_h^{\min}|, \omega_h + |\mathbf{\Omega}_h^{\max}|)$ for $\Delta_{Ah} > 0$ [Fig. 4(a)] and the region $(\omega_h - |\mathbf{\Omega}_h^{\max}|, \omega_h - |\mathbf{\Omega}_h^{\min}|)$ for $\Delta_{Ah} < 0$ [Fig. 4(b)]. Furthermore, the amplitude of the inversion modulation also depends on the initial phase

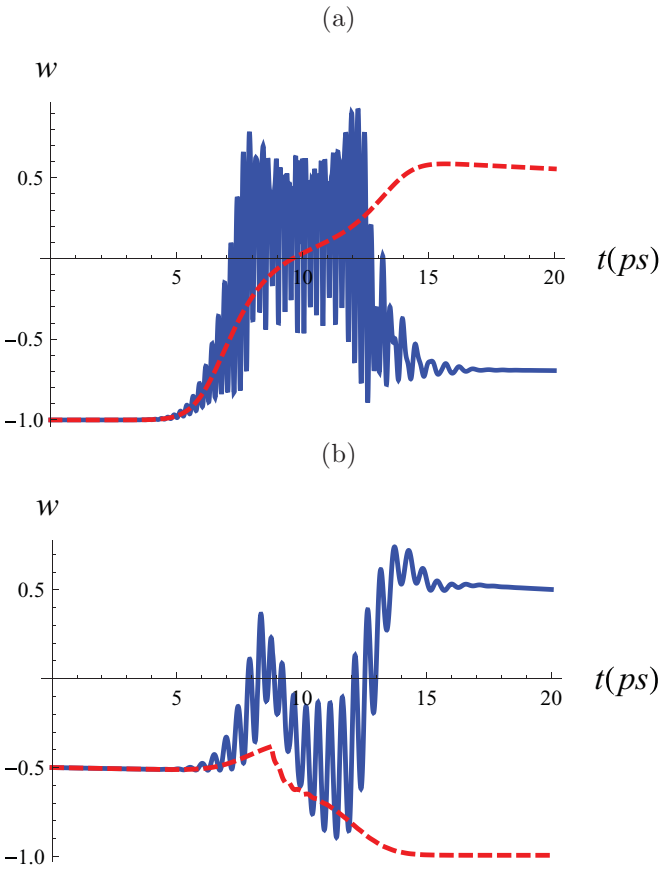

FIG. 3. (Color online) Single-pulse dynamic population switching effects (dashed lines) when only the holding pulse ϵ_h is present ($\epsilon_s = 0$) with (a) $\Delta_{Ah} > 0$ ($\Delta_{Ah} = 11$ THz, $\Delta_{hE} = \omega_h - \omega_E = 4$ THz, $\epsilon_h^{\max} = 20$ THz, $\epsilon_s^{\max} = \epsilon_h^{\max}/3$) and (b) $\Delta_{Ah} < 0$ ($\Delta_{Ah} = -11$ THz, $\Delta_{hE} = 15$ THz, $\epsilon_h^{\max} = 6$ THz, $\epsilon_s^{\max} = 1.25$ THz). The simultaneous introduction of an additional signal pulse ϵ_s to interact with the quantum dot induces significant modulation of the final inversion (solid lines) with (a) $\delta_s = 25$ THz and (b) $\delta_s = -13$ THz. The pulse duration $\tau = 5$ ps, $\gamma = 2.5$ THz, $\gamma_{\text{low}} = 5$ GHz, and $\gamma_p = 0$. For schematic visualizations of the various frequency scales in (a) and (b), see Figs. 13(a) and 14, respectively.

difference $\Delta\phi(t = 0) = \phi_s$ between the signal and holding pulses in certain detuning δ_s ranges. In Fig. 4, the solid curves correspond to $\phi_s = 0$ and the dashed curves correspond to $\phi_s = \pi$.

The phase sensitivity of the inversion modulation is only significant when the detuning δ_s is small, and it results from the interference between the two driving pulses. When δ_s is small, the number of beatings due to interference within the pulse duration is small, making the initial relative phase important for the evolution of the Bloch vector. To see this more clearly, consider the limit $\delta_s \to 0$ (two pulses with the same frequency), where the doubly driven system reduces to a singly driven dynamic switching system with the pulse Rabi frequency being either $\epsilon = \epsilon_h + \epsilon_s$ (when $\phi_s = 0$) or $\epsilon = \epsilon_h - \epsilon_s$ (when $\phi_s = \pi$). This results in significant difference in the final inversion reached between the two different initial phases.

When δ_s increases, there is less phase sensitivity since the increased number of interference cycles tends to average

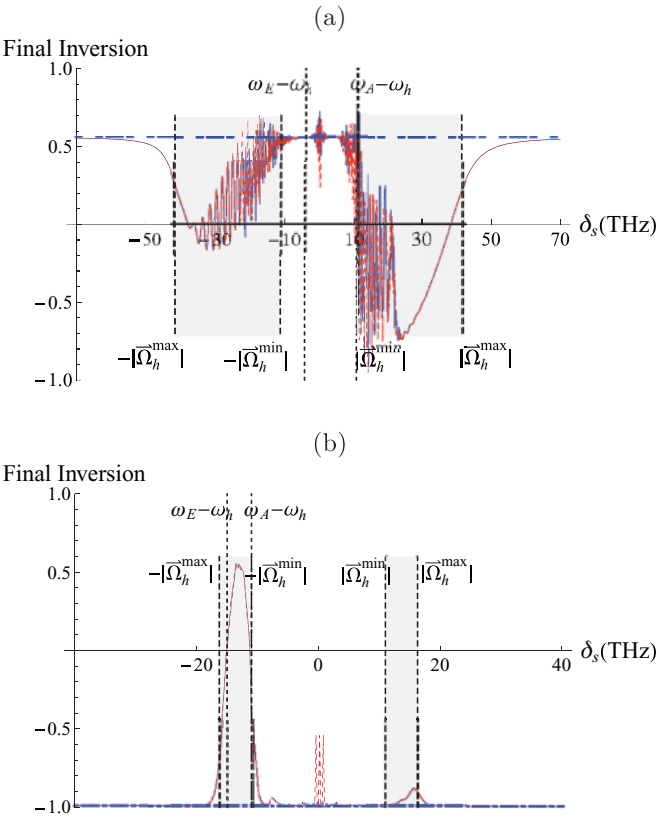

FIG. 4. (Color online) Bichromatic modulation of the final inversion w as function of δ_s. The pulse duration $\tau = 5$ ps, $\gamma_{\text{high}} = 2.5$ THz, $\gamma_{\text{low}} = 5$ GHz, and $\gamma_p = 0$. The (blue) solid curves correspond to $\phi_s = 0$ and (red) dashed curves correspond to $\phi_s = \pi$. (a) Red detuned $\Delta_{Ah} = 11$ THz, $\Delta_{hE} = 4$ THz, $\epsilon_h^{\max} = 20$ THz, and $\epsilon_s^{\max} = \epsilon_h^{\max}/3$. (b) Blue detuned $\Delta_{Ah} = -11$ THz, $\Delta_{hE} = 15$ THz, $\epsilon_h^{\max} = 6$ THz, and $\epsilon_s^{\max} = 1.25$ THz.

out the influence of the initial phase on the quantum-dot evolution. When $\delta_s \gg \tau^{-1}$, the number of interference cycles within the pulse duration is sufficiently large that the effect of relative phase is completely averaged out over time and only the phase-insensitive response remains. Moreover, this phase-insensitive inversion modulation increases as the signal pulse moves away in frequency from the holding pulse and approaches the Mollow sideband regions generated by the holding pulse. Since the signal pulse is weak compared with the holding pulse, it is treated as a perturbation to the dressed-state levels generated by the holding pulse. The strong inversion modulation occurs when there is resonance between the signal pulse and the dressed level transitions that produce the Mollow sidebands. As we have already seen in Fig. 4, when δ_s falls in the Mollow sideband regions $(|\mathbf{\Omega}_h^{\min}|, |\mathbf{\Omega}_h^{\max}|)$ [for $\Delta_{Ah} > 0$, Fig. 4(a)] and $(-|\mathbf{\Omega}_h^{\max}|, -|\mathbf{\Omega}_h^{\min}|)$ [for $\Delta_{Ah} < 0$, Fig. 4(b)], the inversion modulation actually becomes so large that, given proper Δ_{Ah} and $\epsilon_{h,s}$, it is possible to reverse the sign of the final population compared with that produced by the holding pulse alone. We show in the following that population reversal is the result of the rapid steady-state attraction (radiative relaxation) near the peak of the two pulses followed by a complex coherent interaction between the pulses and the QD as the pulses subside. This coherent interaction can be described as an adiabatic following process in the presence of a chirped resonant interaction between the signal pulse and the time-varying Mollow sidebands induced by the holding pulse.

A. Signal-pulse negation of dynamic inversion

We consider the large inversion modulation depicted in Fig. 4(a), focusing on the region of the right Mollow sideband trajectory $(\omega_h + |\mathbf{\Omega}_h^{\min}|, \omega_h + |\mathbf{\Omega}_h^{\max}|)$. The simultaneous arrival of a weak signal pulse negates the final population inversion that would be created by a redshifted $(\Delta_{Ah} > 0)$ holding pulse. Here, the signal pulse is nearly resonant with the right Mollow sideband generated by the holding pulse. To describe this phenomenon, we denote the dressed QD states generated by holding pulse alone as

$$\begin{aligned} |1\rangle_\alpha &= c_\alpha|1\rangle + s_\alpha|2\rangle, \\ |2\rangle_\alpha &= -s_\alpha|1\rangle + c_\alpha|2\rangle, \end{aligned} \tag{10}$$

where

$$\begin{aligned} c_\alpha^2 &= (1 + \Delta_{Ah}/|\mathbf{\Omega}_h|)/2, \\ s_\alpha^2 &= (1 - \Delta_{Ah}/|\mathbf{\Omega}_h|)/2. \end{aligned} \tag{11}$$

The corresponding expectation value of the dipolar and population operators of these singly dressed states are defined as follows:

$$\begin{aligned} u_\alpha &= \langle(|1\rangle_\alpha\langle 2|_\alpha + |2\rangle_\alpha\langle 1|_\alpha)\rangle = \left(c_\alpha^2 - s_\alpha^2\right)u + 2c_\alpha s_\alpha w, \\ v_\alpha &= \langle i(|1\rangle_\alpha\langle 2|_\alpha - |2\rangle_\alpha\langle 1|_\alpha)\rangle = v, \\ w_\alpha &= \langle(|2\rangle_\alpha\langle 2|_\alpha - |1\rangle_\alpha\langle 1|_\alpha)\rangle = -2c_\alpha s_\alpha u + \left(c_\alpha^2 - s_\alpha^2\right)w. \end{aligned} \tag{12}$$

Here, the amplitudes (u, v, w) represent the atomic Bloch vector in the bare-state basis. We can easily identify $(c_\alpha^2 - s_\alpha^2) = \frac{\Delta_{Ah}}{|\mathbf{\Omega}_h|} = \cos\alpha$ and $2c_\alpha s_\alpha = \frac{2\epsilon_h}{|\mathbf{\Omega}_h|} = \sin\alpha$, with α being the angle between the w axis and $\mathbf{\Omega}_h$. This implies $s_\alpha = \sin(\alpha/2)$ and $c_\alpha = \cos(\alpha/2)$. Equation (12) now becomes

$$\begin{aligned} u_\alpha &= u\cos\alpha + w\sin\alpha, \\ w_\alpha &= -u\sin\alpha + w\cos\alpha, \\ v_\alpha &= v, \end{aligned} \tag{13}$$

which is equivalent to a rotational transformation of the (u, v, w) coordinate about the v axis by angle α [Fig. 5(a)]. In the following, this singly dressed state coordinate is called the α coordinate. Now, we further rotate the α coordinate by angle $\phi = \delta_s t + \phi_s$ about the w_α axis so that the coordinate system catches up the rotation of $\mathbf{\Omega}_s$ induced by the frequency difference δ_s between the holding pulse and the signal pulse [Fig. 5(b)]. This transformation brings the reference frame of the Bloch vector to the rotating frame of the signal pulse at ω_s, with the new ϕ coordinate defined as

$$\begin{aligned} u_\phi &= u_\alpha\cos\phi + v_\alpha\sin\phi, \\ v_\phi &= -u_\alpha\sin\phi + v_\alpha\cos\phi, \\ w_\phi &= w_\alpha. \end{aligned} \tag{14}$$

We are especially interested in the final bare quantum-dot population w after interacting with the holding and signal pulses. Since $\alpha = \sin^{-1}(2\epsilon_h/|\mathbf{\Omega}_h|) \to 0$ as $\epsilon_h \to 0$ after the

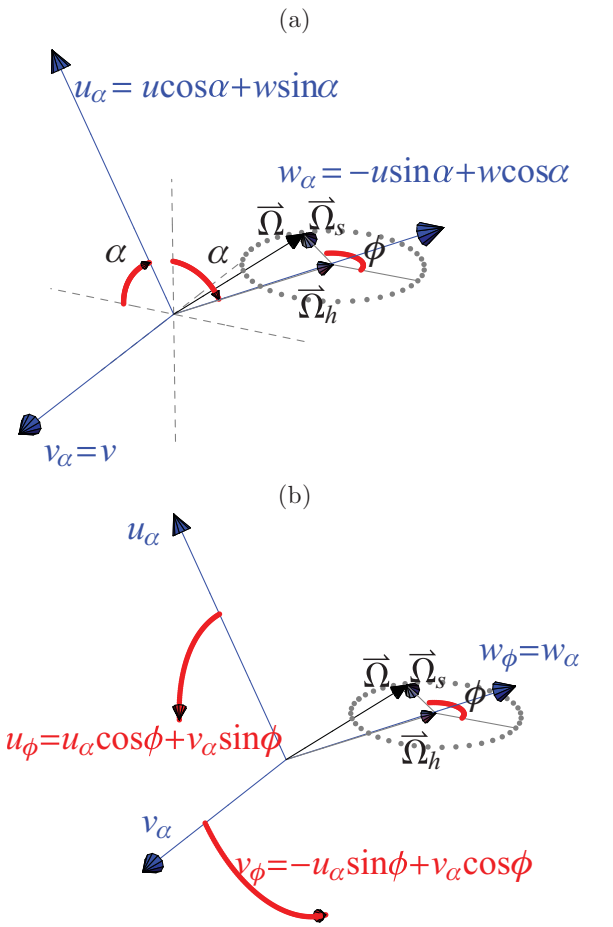

FIG. 5. (Color online) Bloch coordinate transformations for $\Delta_{Ah} > 0$ case. The original (u,v,w) coordinate system in the bare atomic basis is (a) first rotated by angle α about the v axis to parallel alignment with $\mathbf{\Omega}_h$ (dressed-state basis of the holding pulse), and then (b) rotated by angle ϕ about the w_α axis to catch up with the rotation of the signal-pulse torque vector $\mathbf{\Omega}_s$.

passage of the pulses and $w_\phi = w_\alpha \to w$, the final inversion in the ϕ coordinate also represents the final inversion in the bare atomic states.

Equations (13) and (14) are basis transformations with no approximation introduced. The transformed Bloch equation in the ϕ coordinate becomes

$$\dot{\boldsymbol{\rho}}_\phi = \mathbf{\Omega}_\phi \times \boldsymbol{\rho}_\phi - \Gamma_\phi + \mathbf{C}_\phi, \tag{15}$$

where

$$\mathbf{C}_\phi = \begin{pmatrix} \cos\phi(V\cos\alpha - \Gamma_w\sin\alpha) \\ -\sin\phi(V\cos\alpha - \Gamma_w\sin\alpha) \\ -V\sin\alpha - \Gamma_w\cos\alpha \end{pmatrix},$$

$$\mathbf{\Omega}_\phi = \begin{pmatrix} -2\epsilon_s(\sin^2\phi + \cos^2\phi\cos\alpha) \\ 0 \\ |\mathbf{\Omega}_h| - \delta \end{pmatrix} + 2\epsilon_s\cos\phi \begin{pmatrix} 0 \\ -\sin\phi(1-\cos\alpha) \\ \sin\alpha \end{pmatrix} + \dot{\alpha}\begin{pmatrix} \sin\phi \\ \cos\phi \\ 0 \end{pmatrix},$$

and $\Gamma_\phi = \left(\gamma_\phi^u, \gamma_\phi^v, \gamma_\phi^w\right)$, with

$$\begin{aligned}
\gamma_\phi^u &= -(\Gamma_u\cos^2\alpha\cos^2\phi + \Gamma_v\sin^2\phi + \Gamma_w\cos^2\phi\sin^2\alpha \\
&\quad - V\cos\alpha\sin\alpha\cos^2\phi)u_\phi \\
&\quad + (\Gamma_u\cos^2\alpha\cos\phi\sin\phi - \Gamma_v\cos\phi\sin\phi \\
&\quad + \Gamma_w\cos\phi\sin\phi\sin^2\alpha)v_\phi \\
&\quad + [(\Gamma_u - \Gamma_w)\cos\alpha\sin\alpha\cos\phi - V\sin^2\alpha\cos\phi]w_\phi, \\
\gamma_\phi^v &= \cos\phi\sin\phi(\Gamma_u\cos^2\alpha - \Gamma_v + \Gamma_w\sin^2\alpha - V\cos\alpha\sin\alpha)u_\phi \\
&\quad - (\Gamma_u\cos^2\alpha\sin^2\phi + \Gamma_v\cos^2\phi + \Gamma_w\sin^2\alpha\sin^2\phi \\
&\quad - V\cos\alpha\sin\alpha\sin^2\phi V)v_\phi \\
&\quad - \sin\phi(\Gamma_u\cos\alpha\sin\alpha - \Gamma_w\cos\alpha\sin\alpha - V\sin^2\alpha)w_\phi, \\
\gamma_\phi^w &= \cos\phi(\Gamma_u\cos\alpha\sin\alpha - \Gamma_w\cos\alpha\sin\alpha + V\cos^2\alpha)u_\phi \\
&\quad - \sin\phi(\Gamma_u\cos\alpha\sin\alpha - \Gamma_w\cos\alpha\sin\alpha + V\cos^2\alpha)v_\phi \\
&\quad - (\Gamma_u\sin^2\alpha + \Gamma_w\cos^2\alpha + V\cos\alpha\sin\alpha)w_\phi.
\end{aligned}$$

Now we introduce an approximation to simplify this Bloch equation. When $|\delta_s| \gg \tau^{-1}$, the two-pulse interference time scale becomes much smaller than other time scales in Eq. (15). In this case, it is appropriate to replace periodic functions in ϕ with their time averages ($\overline{\sin\phi} = \overline{\cos\phi} = 0$, and $\overline{\sin^2\phi} = \overline{\cos^2\phi} = 1/2$) in Eq. (15), while assuming all other terms to be approximately constant during the average. Then, the time-averaged Bloch equation in the ϕ coordinate reads as

$$\dot{\boldsymbol{\rho}}_\phi = \mathbf{\Omega}_{\langle\phi\rangle} \times \boldsymbol{\rho}_\phi - \Gamma_{\langle\phi\rangle} + \mathbf{C}_{\langle\phi\rangle}, \tag{16}$$

where

$$\begin{aligned}
\mathbf{\Omega}_{\langle\phi\rangle} &= (-\epsilon_s(1+\cos\alpha), 0, |\mathbf{\Omega}_h| - \delta_s), \\
\Gamma_{\langle\phi\rangle} &= \left(u_\phi\gamma_{\langle\phi\rangle}^u, v_\phi\gamma_{\langle\phi\rangle}^v, w_\phi\gamma_{\langle\phi\rangle}^w\right), \\
\mathbf{C}_{\langle\phi\rangle} &= (0, 0, -V\sin\alpha - \Gamma_w\cos\alpha)
\end{aligned}$$

with $\gamma_{\langle\phi\rangle}^u = \gamma_{\langle\phi\rangle}^v = (\Gamma_u\cos^2\alpha + \Gamma_v + \Gamma_w\sin^2\alpha - V\cos\alpha\sin\alpha)/2$ and $\gamma_{\langle\phi\rangle}^w = \Gamma_u\sin^2\alpha + \Gamma_w\cos^2\alpha + V\cos\alpha\sin\alpha$.

Similar to a singly driven system with a torque vector $\mathbf{\Omega} = (2\epsilon, 0, \Delta_{AL})$ [10,11], the coherent interaction (cross product) in Eq. (16) is determined by a torque vector $\mathbf{\Omega}_{\langle\phi\rangle}$ with its u_ϕ component proportional to the signal field Rabi frequency ϵ_s, and its v_ϕ component identically zero. The interesting difference from the Bloch equation of a singly driven system, however, comes from the w_ϕ component of $\mathbf{\Omega}_{\langle\phi\rangle}$. In place of the atom-field detuning Δ_{AL} in the torque vector $\mathbf{\Omega}$ of a singly driven system [10,11], there appears an effective detuning $\Delta_{+s} = |\mathbf{\Omega}_h| - \delta_s = (\omega_h + |\mathbf{\Omega}_h|) - \omega_s$ that represents the detuning between the signal-pulse carrier frequency ω_s and the right Mollow sideband with frequency $\omega_h + |\mathbf{\Omega}_h|$ [see Fig. 7(a)]. Due to the dependence of the Mollow splitting $|\mathbf{\Omega}_h|$ on the holding-pulse field strength, an effective chirping of the detuning Δ_{+s} occurs during the passage of the pulses. This leads to the large inversion modulation of the quantum-dot population when the signal-pulse frequency is near the right Mollow sideband, as demonstrated below.

As shown in Fig. 6(a), after the passage of a single redshifted holding pulse ($\Delta_{Ah} > 0$), the Bloch vector of the quantum dot evolves to state $\boldsymbol{\rho}(t_3)$ with positive population inversion. This is the result of an enhanced radiative relaxation of the

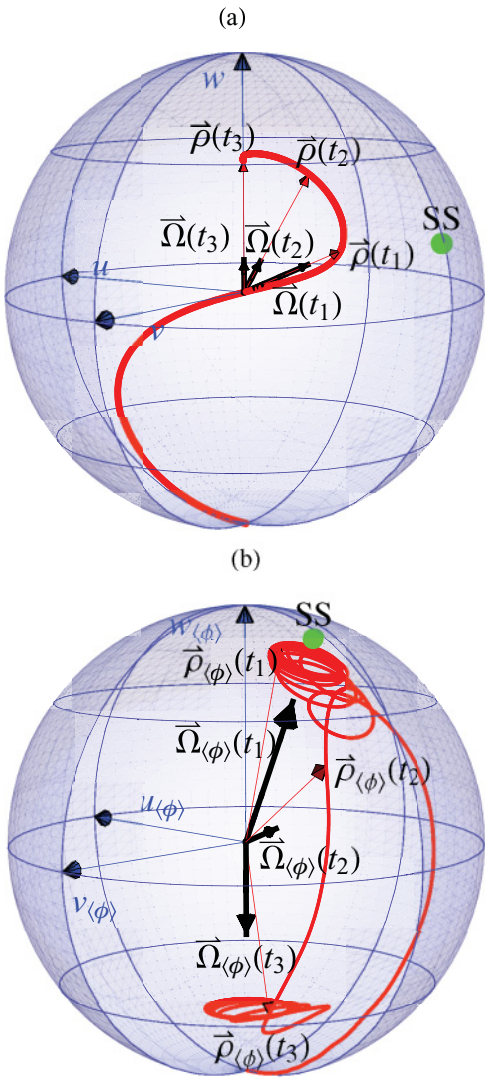

FIG. 6. (Color online) Population inversion modulation when $\Delta_{Ah} > 0$. The pulse duration $\tau = 5$ ps, $\gamma_{\text{high}} = 2.5$ THz, $\gamma_{\text{low}} = 5$ GHz, $\gamma_p = 0$, $\Delta_{Ah} = 11$ THz, $\Delta_{hE} = 4$ THz, $\delta_s = 23$ THz, and $\epsilon_h^{\max} = 20$ THz. (a) When $\epsilon_s^{\max} = 0$, positive inversion is obtained through dynamic inversion in the (u,v,w) frame. (b) When $\epsilon_s^{\max} = \epsilon_h^{\max}/3$, negative inversion is obtained via dressed-state chirping in the (u_ϕ, v_ϕ, w_ϕ) frame.

Bloch vector $\boldsymbol{\rho}$ toward the instantaneous steady state [large (green) dot SS] at the peak of the pulse (t_1) followed by adiabatic following by the Bloch vector $\boldsymbol{\rho}$ of the torque vector $\boldsymbol{\Omega}$ to the inverted state [10,11]. This positive final inversion is dramatically changed when a weaker secondary signal pulse passes the quantum dot at the same time as the holding pulse, especially when the signal-pulse frequency is near the right Mollow sideband generated by the holding pulse [Fig. 4(a)]. In this case, a negative final inversion is reached instead. The negation of the final inversion by the signal pulse is the result of the Bloch dynamics shown in Fig. 6(b), described by the time-averaged Bloch equation (16) in the $(u_{\langle\phi\rangle}, v_{\langle\phi\rangle}, w_{\langle\phi\rangle})$ frame. Near the peak of the pulse, the field-enhanced radiative relaxation rates cause rapid attraction to the steady state of Eq. (16) [large (green) dot SS in Fig. 6(b)] and bring the Bloch vector close to SS at t_1. At this time,

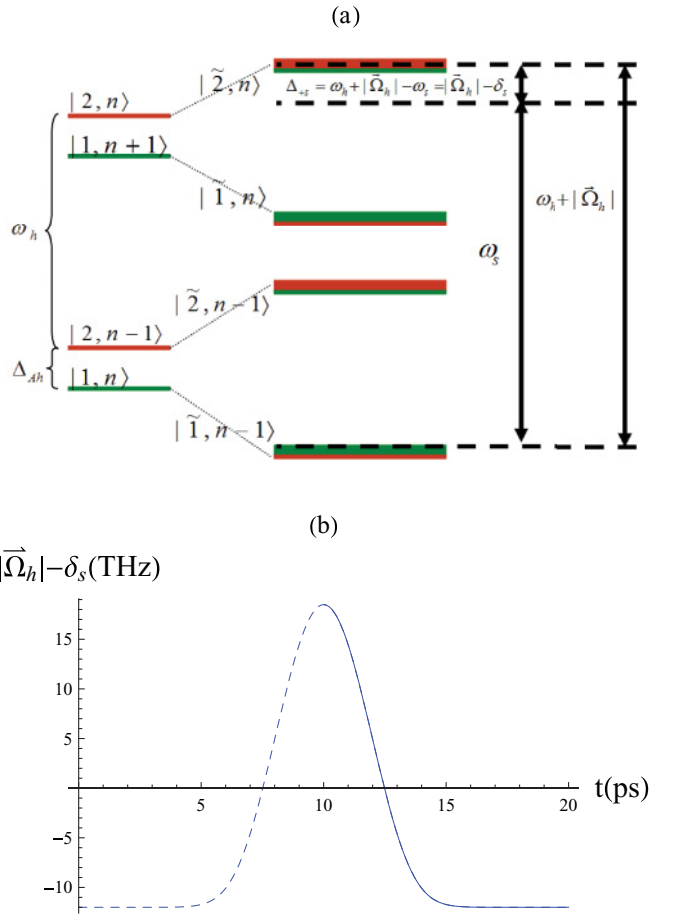

FIG. 7. (Color online) Chirping of the detuning between the signal pulse and the singly dressed levels transition that gives rise to the right Mollow sideband. The pulse duration $\tau = 5$ ps, $\gamma_{\text{high}} = 2.5$ THz, $\gamma_{\text{low}} = 5$ GHz, $\gamma_p = 0$, $\Delta_{Ah} = 11$ THz, $\Delta_{hE} = 4$ THz, $\delta_s = 23$ THz, and $\epsilon_h^{\max} = 20$ THz. (a) Dressed-state levels and the detuning δ_{+s} between the signal pulse and the right Mollow sideband of the holding pulse. (b) Effective chirping of δ_{+s} over time.

the torque vector $\boldsymbol{\Omega}_{\langle\phi\rangle}(t_1)$ also points to SS with its detuning component $\Delta_{+s} = |\boldsymbol{\Omega}_h| - \delta_s$ being positive at the peak of the pulse [Fig. 7(b)]. As the pulse subsides, the relaxation rate drops significantly and the system enters the coherent transient time regime. The decrease in holding-pulse Rabi frequency means the detuning Δ_{+s} also decreases, corresponding to an effective chirping of the signal with respect to the right Mollow sideband. If δ_s satisfies $\Delta_{Ah} = |\boldsymbol{\Omega}_h^{\min}| < \delta_s < |\boldsymbol{\Omega}_h^{\max}|$ [the region $(\omega_h + |\boldsymbol{\Omega}_h^{\min}|, \omega_h + |\boldsymbol{\Omega}_h^{\max}|)$ indicated in Fig. 4(a)], then the effective chirping moves the torque vector $\boldsymbol{\Omega}_{\langle\phi\rangle}$ from pointing upward at pulse peak to pointing downward at t_3 [$\Delta_{+s} < 0$ at the end of the pulse, see Fig. 7(b)]. If, furthermore, the signal pulse is strong enough to satisfy the adiabatic condition (torque vector speed is much smaller than the precession frequency of the Bloch vector around the torque vector [10,11])

$$\left|\frac{d\boldsymbol{\Omega}_{\langle\phi\rangle}}{dt}\right| \ll |\boldsymbol{\Omega}_{\langle\phi\rangle}|, \tag{17}$$

then the Bloch vector will follow the chirping movement of the torque vector and reach a state without inversion, even though the holding pulse alone would produce inversion.

B. Signal-pulse negation of dynamic de-excitation

We now consider the large inversion modulation effect depicted in the left Mollow sideband region ($\omega_h - |\mathbf{\Omega}_h^{\max}|, \omega_h - |\mathbf{\Omega}_h^{\min}|$) of Fig. 4(b). Here, the simultaneous presence of a weak signal pulse modulates the final population inversion reached after the passage of a blueshifted holding pulse ($\Delta_{Ah} < 0$) from negative to positive. In this case, the signal pulse is nearly resonant with the left Mollow sideband generated by the blueshifted holding pulse. As in the previous section, we explain this inversion modulation effect by transforming the Bloch equation (9) into the ϕ-coordinate system through the rotations defined in Eqs. (13) and (14). However, a subtle difference from the previous section arises in the definition of angle α. If we continue defining $\cos\alpha = \Delta_{Ah}/|\mathbf{\Omega}_h|$ and $\sin\alpha = 2\epsilon_h/|\mathbf{\Omega}_h|$ as we did for a redshifted holding pulse, then the final population inversion $w_\phi = w_\alpha = -u\sin\alpha + w\cos\alpha \to -w$ instead of w after the passage of the pulses. This can be easily seen from $\sin\alpha \to 0$ and $\cos\alpha \to -1$ as $\epsilon_s \to 0$, which implies $\alpha \to \pi$ because the torque vector $\mathbf{\Omega}_h$ points downward for $\Delta_{Ah} < 0$. In order to ensure that $w_\phi \to w$ as it must after the pulse subsides, we must choose $\cos\alpha = -\Delta_{Ah}/|\mathbf{\Omega}_h| = |\Delta_{Ah}|/|\mathbf{\Omega}_h|$ and $\sin\alpha = -2\epsilon_h/|\mathbf{\Omega}_h|$ in the rotation transformation (13). The subsequent transformation to the ϕ coordinate, however, is identical to the $\Delta_{Ah} > 0$ case, and is depicted in Fig. 8(b).

After the coordinate rotations of Eqs. (13) and (14), followed by the time average of the ϕ oscillatory terms over the time scale δ_s^{-1}, the transformed Bloch equation for blueshifted holding pulse and a signal pulse has the same form as Eq. (16), except for the expression of $\mathbf{\Omega}_{\langle\phi\rangle}$. This now becomes $\mathbf{\Omega}_{\langle\phi\rangle} = -|\mathbf{\Omega}_h| - \delta_s = (\omega_h - |\mathbf{\Omega}_h|) - \omega_s = \Delta_{-s}$ and represents the detuning of the signal-pulse carrier frequency from the left Mollow sideband generated by the holding pulse [Fig. 10(a)]. As we show below, the chirping of Δ_{-s} gives rise to the large inversion modulation of the quantum-dot population when the signal-pulse frequency is near the left Mollow sideband generated by a blueshifted holding pulse.

It can be seen from Fig. 9(a) that, after the passage of a single blueshifted holding pulse ($\Delta_{Ah} < 0$), the Bloch vector $\boldsymbol{\rho}(t_3)$ of the quantum dot evolves to the ground state. This is enabled, as before, by steady-state attraction and adiabatic following as shown in Fig. 9(a) [10,11]. This de-excitation is negated when a secondary signal pulse passes the quantum dot at the same time as the holding pulse, provided that the signal pulse frequency is near the left Mollow sideband generated by the holding pulse [Fig. 4(b)]. The positive final inversion caused by the signal pulse is the result of the Bloch dynamics shown in Fig. 9(b) in the $(u_{\langle\phi\rangle}, v_{\langle\phi\rangle}, w_{\langle\phi\rangle})$ frame. Near the peak of the pulse, the field-enhanced radiative relaxation causes rapid attraction to the steady state of Eq. (16) [large (green) dot SS in Fig. 9(b)] and brings the Bloch vector close to SS at t_1. At this time, the torque vector $\mathbf{\Omega}_{\langle\phi\rangle}(t_1)$ also points approximately to SS with negative detuning component Δ_{-s} [Fig. 10(b)]. As the pulse subsides, the relaxation rate drops significantly and the system enters the coherent transient time regime.

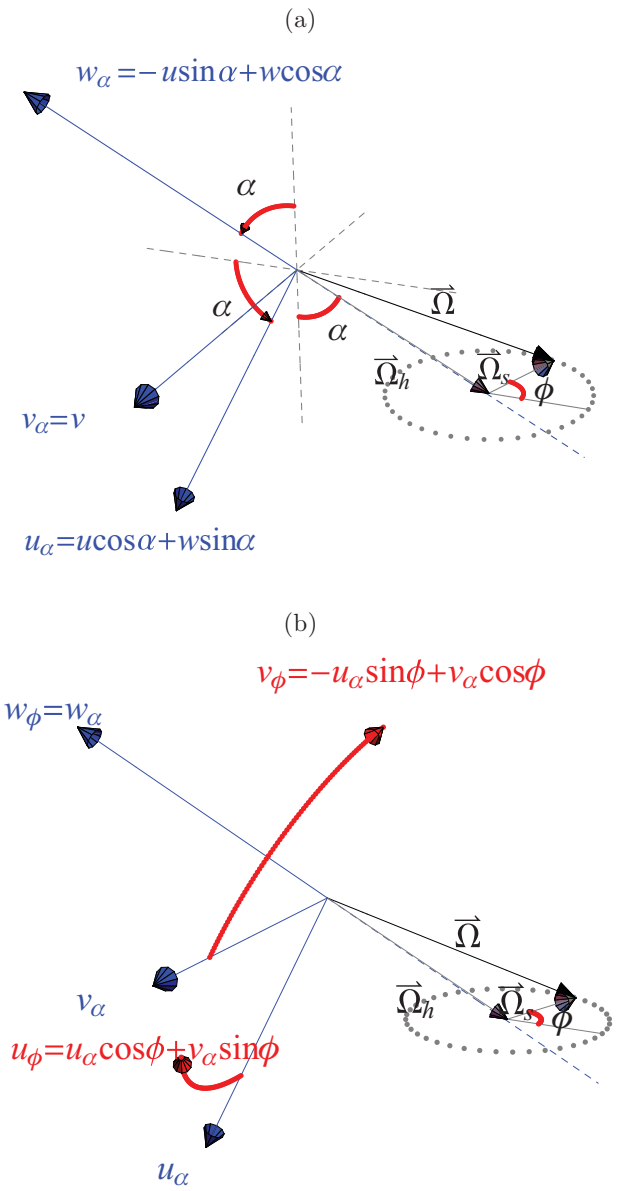

FIG. 8. (Color online) Bloch coordinate transformations for $\Delta_{Ah} < 0$ case. The original (u, v, w) coordinate system in the bare atomic basis is (a) first rotated by angle α about the v axis to antiparallel alignment with $\mathbf{\Omega}_h$ (dressed-state basis of the holding pulse), and then (b) rotated by angle ϕ about the w_α axis to catch up with the rotation of the signal-pulse torque vector $\mathbf{\Omega}_s$.

The decrease in holding-pulse Rabi frequency means that the detuning Δ_{-s} increases, corresponding to an effective chirping of the left Mollow sideband. If δ_s satisfies $\Delta_{Ah} = -|\mathbf{\Omega}_h^{\max}| < \delta_s < -|\mathbf{\Omega}_h^{\min}|$ [see Fig. 4(b)], then the effective chirping moves the torque vector $\mathbf{\Omega}_{\langle\phi\rangle}$ from pointing downward at pulse peak to pointing upward at t_3 [$\Delta_{-s} > 0$ at the end of the pulse [see Fig. 10(b)]. If the adiabatic following condition of the signal pulse [Eq. (17)] is satisfied, then the Bloch vector will follow the chirping movement of the torque vector and reach a final inverted state.

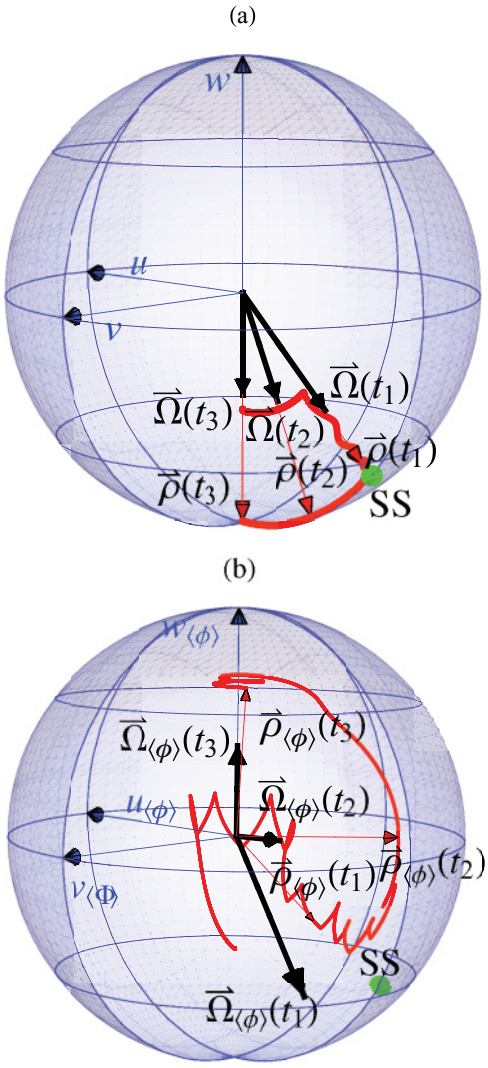

FIG. 9. (Color online) Population inversion modulation when $\Delta_{Ah} < 0$. The pulse duration $\tau = 5$ ps, $\gamma_{\text{high}} = 2.5$ THz, $\gamma_{\text{low}} = 5$ GHz, $\gamma_p = 0$, $\Delta_{Ah} = -11$ THz, $\Delta_{hE} = 15$ THz, $\delta_s = -13$ THz, and $\epsilon_h^{\max} = 6$ THz. (a) When $\epsilon_s^{\max} = 0$, negative inversion is obtained through dynamic inversion in the (u,v,w) frame. (b) When $\epsilon_s^{\max} = 1.25$ THz, positive inversion is obtained via dressed-state chirping in the (u_ϕ, v_ϕ, w_ϕ) frame.

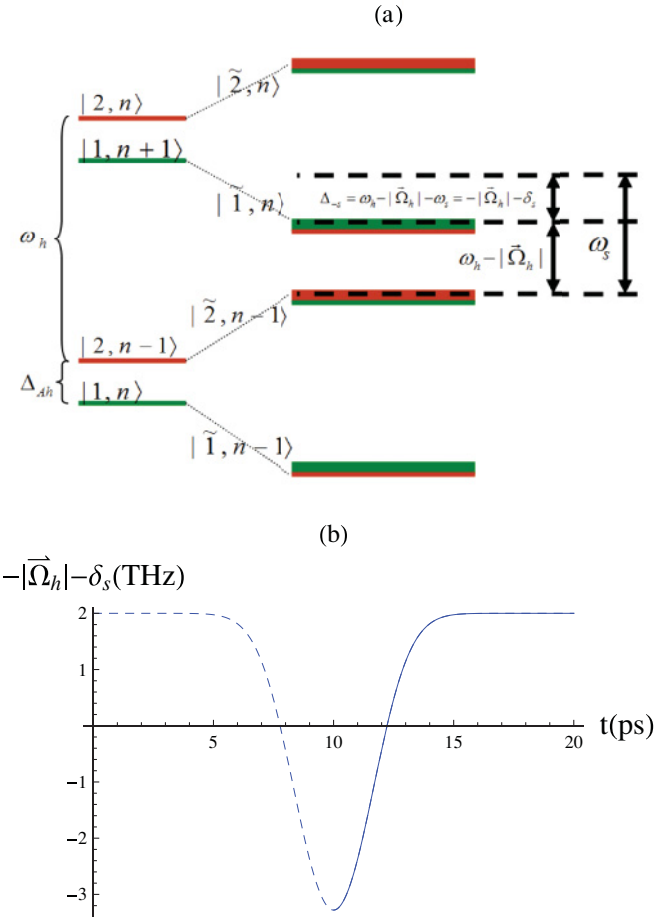

FIG. 10. (Color online) Chirping of the detuning between the signal pulse and the singly dressed levels transition that gives rise to the right Mollow sideband. The pulse duration $\tau = 5$ ps, $\gamma_{\text{high}} = 2.5$ THz, $\gamma_{\text{low}} = 5$ GHz, $\gamma_p = 0$, $\Delta_{Ah} = -11$ THz, $\Delta_{hE} = 15$ THz, $\delta_s = -13$ THz, and $\epsilon_h^{\max} = 6$ THz. (a) Dressed-state levels and the detuning δ_{-s} between the signal pulse and the left Mollow sideband of the holding pulse. (b) Effective chirping of δ_{-s} over time.

C. The time-average approximation of the Bloch equation

Our explanation of the bichromatic inversion modulation effect in Secs. III A and III B is based on the time-average approximation used to simplify the Bloch equation (15) into the intuitive form (16). In Figs. 11 and 12, we verify the validity of this time-average approximation by comparing the numerical solutions of the Bloch equation (15) (solid lines) and the approximate Bloch equation (16) (dashed lines) for both redshifted (Fig. 11) and blueshifted (Fig. 12) holding pulses.

Clearly, Eq. (16) is a good approximation for describing the final population inversion w_ϕ reached after passage of the pulses. Although the time-average operation reduces the oscillation amplitude of u_ϕ after the passage of a redshifted pulse (Fig. 11), it provides a reliable picture of dressed-state chirping Bloch dynamics, and especially the temporal evolution of w_ϕ during passage of the driving pulses.

IV. APPLICATION OF INVERSION MODULATION TO OPTICAL LOGIC

In this section, we demonstrate the use of bichromatic quantum-dot inversion modulation for ultrafast all-optical logic operations, such as AND, OR, and NOT operations. The proposed devices can be realized by embedding a collection of independent quantum dots inside a 20-unit-cell segment of a bimodal 2D-3D PBG waveguide with one cutoff mode [25,26,29]. Ultrafast, intense, optical pulses with two different carrier frequencies pass through the waveguide to interact with the quantum dots. The dot transition frequencies and pulse carrier frequencies are chosen to be close above the LDOS discontinuity introduced by the cutoff frequency. The strong coupling between the quantum dots and the two simultaneous channels of optical pulses leads to quantum-dot population dynamics as demonstrated in the previous sections. The

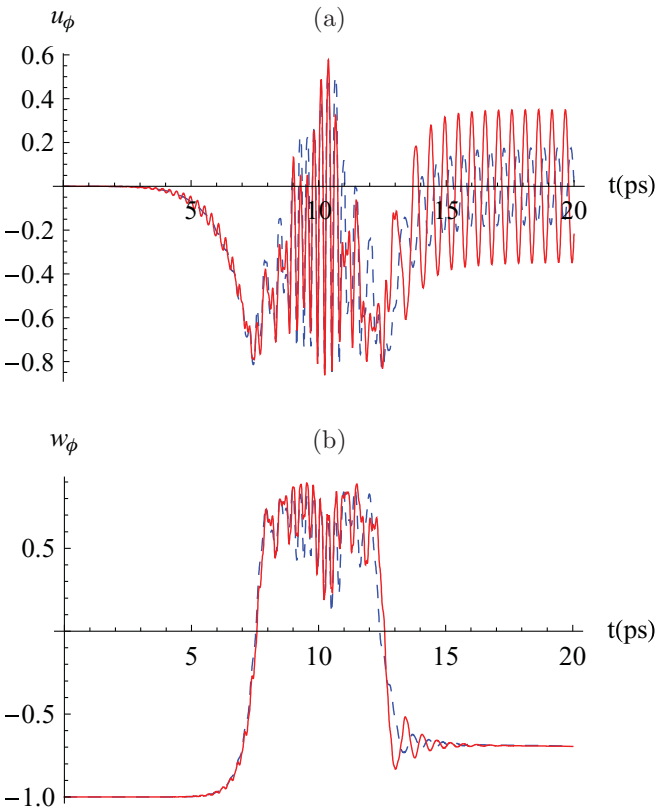

FIG. 11. (Color online) Comparison of the ϕ-coordinate atomic variable evolutions according to the time-averaged Bloch equation (16) (dashed curves) and the unaveraged Bloch equation (15) for (a) u_ϕ and (b) w_ϕ. The pulse duration $\tau = 5$ ps, $\gamma_{\text{high}} = 2.5$ THz, $\gamma_{\text{low}} = 5$ GHz, $\gamma_p = 0$, $\Delta_{Ah} = 11$ THz, $\Delta_{hE} = 4$ THz, $\delta_s = 23$ THz, $\epsilon_h^{\max} = 20$ THz, and $\epsilon_s^{\max} = \epsilon_h^{\max}/3$.

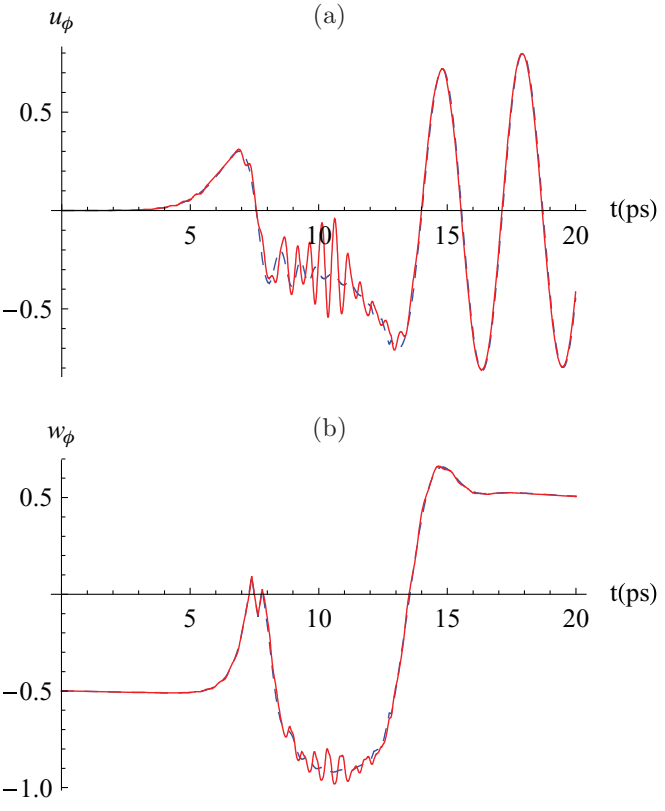

FIG. 12. (Color online) Comparison of the ϕ-coordinate atomic variable evolutions according to the time-averaged Bloch equation (16) (dashed curves) and the unaveraged Bloch equation (15) for (a) u_ϕ and (b) w_ϕ. The pulse duration $\tau = 5$ ps, $\gamma_{\text{high}} = 2.5$ THz, $\gamma_{\text{low}} = 5$ GHz, $\gamma_p = 0$, $\Delta_{Ah} = -11$ THz, $\Delta_{hE} = 15$ THz, $\delta_s = -13$ THz, $\epsilon_h^{\max} = 6$ THz, and $\epsilon_s^{\max} = 1.25$ THz.

sensitive dependence of the final population inversion on the relative strength of the two channels of input optical pulses and their detunings from the quantum-dot transition frequencies can be exploited for all-optical logic. The sign of the final population inversion determines the subsequent amplification or attenuation of a probe pulse. Consequently, the logically determined quantum-dot final state can be translated into all-optical logic relations between the output probe signal and the input signals.

A. All-optical NOT gate

In a logic NOT operation, the output is the opposite of the input. A NOT gate can have only one input and one output. To implement an all-optical NOT operation, consider the spectrum configuration shown in Fig. 13(a). A channel of strong optical holding pulses with carrier frequency ω_h and $\Delta_{Ah} > 0$ is modulated by weaker signal pulses with carrier frequency ω_s that is nearly resonant with the right Mollow sideband ($\Delta_{Ah} = |\mathbf{\Omega}_h^{\min}| < \delta_s < |\mathbf{\Omega}_h^{\max}|$). The channel of optical information at carrier frequency ω_s passes through the quantum dot at the same time as the holding pulses at carrier frequency ω_h. As shown in Fig. 13(b), when the signal is not present (input 0), dynamic inversion results in a final inverted state (excited), whereas when the signal is present (input 1), the final population becomes negative (de-excited) as demonstrated in Sec. III A. The excited quantum dots will allow the passage of the subsequent probe pulse (defined as output 1) near the dot transition frequency ω_A, whereas the de-excited quantum dots will absorb and forbid the passage of the probe pulse (defined as output 0). As a result, an optical input of 0 in frequency channel ω_s leads to an optical output of 1 in frequency channel ω_A, and vice versa. This fulfills the all-optical logic NOT operation.

B. All-optical AND and OR gates

In a logic AND operation, the single output is positive only if both of the two inputs are positive, whereas a logic OR operation results in the single output being positive if either of the two inputs is positive. These two logic operations can be realized with a similar construction to that shown in Fig. 13(a). The spectral configuration of both logic devices is shown in Fig. 14. Two channels of optical information at frequency ω_s pass through the Q dot at the same time as a stronger holding pulse at ω_h with $\Delta_{Ah} < 0$ and $-|\mathbf{\Omega}_h^{\max}| < \delta_s < -|\mathbf{\Omega}_h^{\min}| = \Delta_{Ah}$. Depending on the relative strengths of the holding and signal pulses, the proposed device can utilize the positive inversion modulation (discussed in Sec. III B) to perform either logic AND or OR operations. The modulation response curve of the final QD inversion with respect to ϵ_s depends on the strength of ϵ_h [Figs. 15(b) and 16(b)]. For a relatively large ϵ_h,

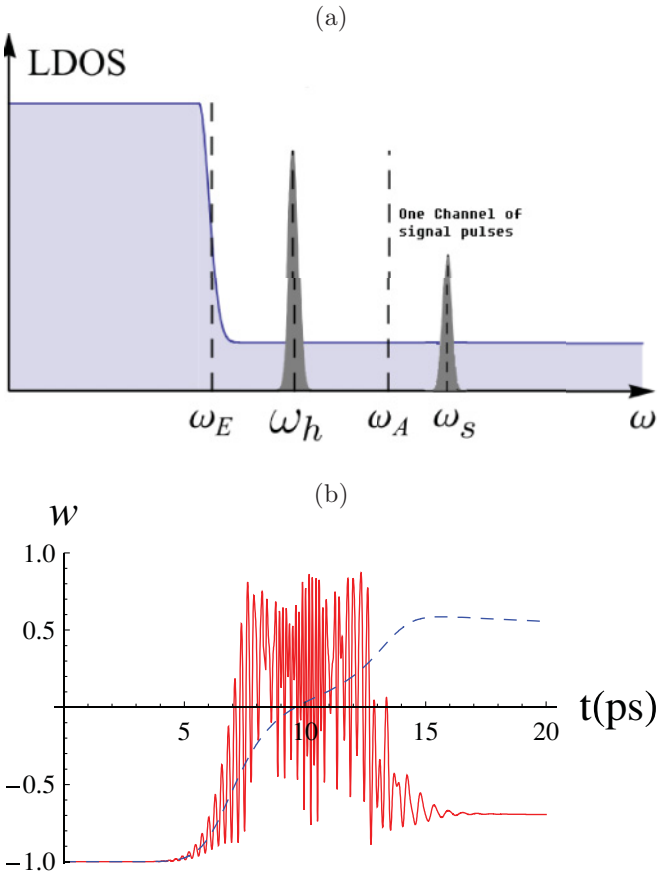

FIG. 13. (Color online) Logic NOT operation via dressed chirping-induced population inversion modulation when $\Delta_{Ah} > 0$. The pulse duration $\tau = 5$ ps, $\gamma_{\text{high}} = 2.5$ THz, $\gamma_{\text{low}} = 5$ GHz, $\gamma_p = 0$, $\Delta_{Ah} = 11$ THz, $\Delta_{hE} = 4$ THz, $\delta_s = 23$ THz, and $\epsilon_h^{\max} = 20$ THz. (a) Spectrum model of the device. (b) Logic operation. The (blue) dashed line corresponds to $\epsilon_s^{\max} = 0$ (input 0) while the (red) solid line corresponds to $\epsilon_s^{\max} = \epsilon_h^{\max}/3$ (input 1).

the final inversion increases monotonically with ϵ_s [Fig. 15(b)], while for a relatively small ϵ_h, the final inversion easily reaches saturation with increasing ϵ_s [Fig. 16(b)]. The former case can be utilized to perform logic AND operations in which only the addition of two signal pulses [input (1,1)] is strong enough to switch the population to positive inversion [Fig. 15(a)]. One

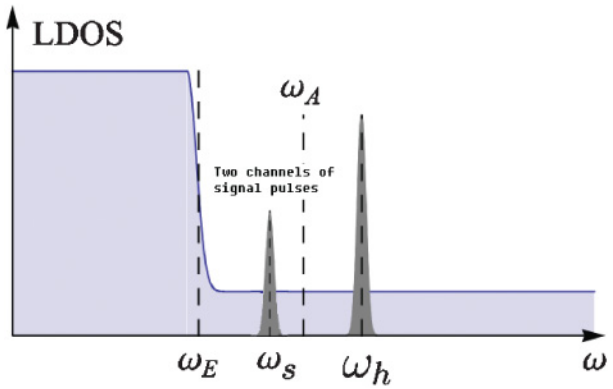

FIG. 14. (Color online) Spectral configuration of the logic AND and OR devices.

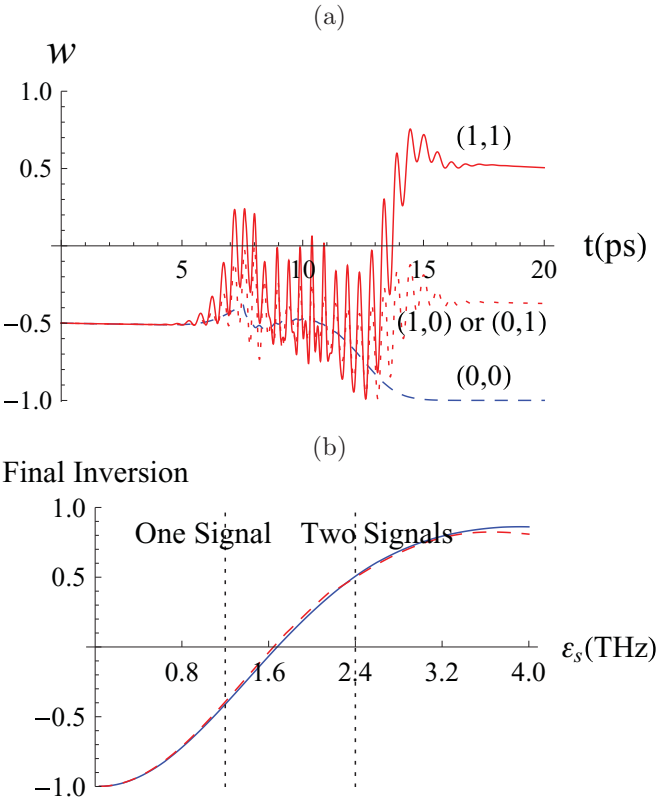

FIG. 15. (Color online) Logic AND gate via dressed chirping-induced population inversion modulation when $\Delta_{Ah} < 0$. The pulse duration $\tau = 5$, $\gamma_{\text{high}} = 2.5$ THz, $\gamma_{\text{low}} = 5$ GHz, $\gamma_p = 0$, $\Delta_{Ah} = -11$ THz, $\Delta_{hE} = 15$ THz, $\delta_s = -13$ THz, and $\epsilon_h^{\max} = 10$ THz. (a) Logic operation. The (blue) dashed curve corresponds to $\epsilon_s^{\max} = 0$ [input (0,0)], the (red) dotted curve corresponds to $\epsilon_s^{\max} = 1.2$ THz [input (0,1) or (1,0)], and the (red) solid curve corresponds to $\epsilon_s^{\max} = 2.4$ THz [input(1,1)]. (b) Plot of final inversion as a function of ϵ_s with $\phi_s = 0$ [(blue) solid curve] and $\phi_s = \pi$ [(red) dashed curve].

the other hand, the latter case can be utilized to perform logic OR operations in which the arrival of only one signal-pulse [input (0,1) or (1,0)] or the simultaneous arrival of both signal pulses [input (1,1)] can switch the population to approximately the same amount of positive inversion [Fig. 16(a)].

C. Inhomogeneous broadening and phonon dephasing: Toward practical devices

The studies presented in the previous sections focus on the response of a single Q dot to the holding and signal pulses. The generalization to a collection of independent Q dots is obtained by taking an average over the individual Q-dot responses. Figure 17 depicts the average inversion modulation as a function of the signal to holding pulse detuning δ_s. Compared with the corresponding single-dot response in Fig. 4, the inhomogeneous broadening tends to smooth out oscillations in the inversion curve and decrease the overall switching contrast.

To demonstrate realistic logic device performance, Fig. 18 shows the logic AND and OR operations when the inhomogeneous broadening is 6 THz (about 0.5% for 1.5 μm transition frequency) and Fig. 19 shows the corresponding performances

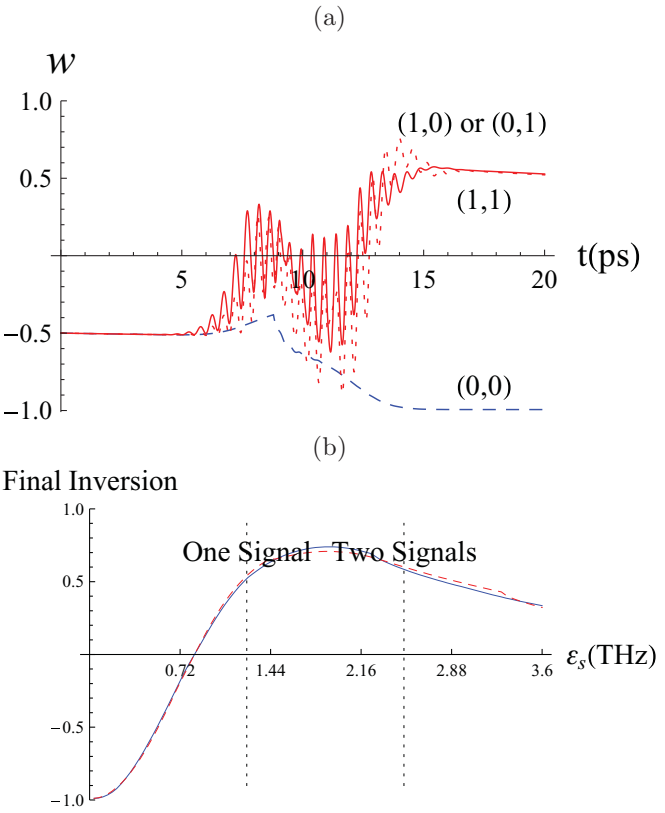

FIG. 16. (Color online) Logic OR gate via dressed chirping-induced population inversion modulation when $\Delta_{Ah} < 0$. The pulse duration $\tau = 5$ ps, $\gamma_{\text{high}} = 2.5$ THz, $\gamma_{\text{low}} = 5$ GHz, $\gamma_p = 0$, $\Delta_{Ah} = -11$ THz, $\Delta_{hE} = 15$ THz, $\delta_s = -13$ THz, and $\epsilon_h^{\max} = 6$ THz. (a) Logic operation. The (blue) dashed curve corresponds to $\epsilon_s^{\max} = 0$ [input (0,0)], the (red) dotted curve corresponds to $\epsilon_s^{\max} = 1.25$ THz [input (0,1) or (1,0)], and the (red) solid curve corresponds to $\epsilon_s^{\max} = 2.5$ THz [input(1,1)]. (b) Plot of final inversion as a function of ϵ_s with $\phi_s = 0$ [(blue) solid curve] and $\phi_s = \pi$ [(red) dashed curve].

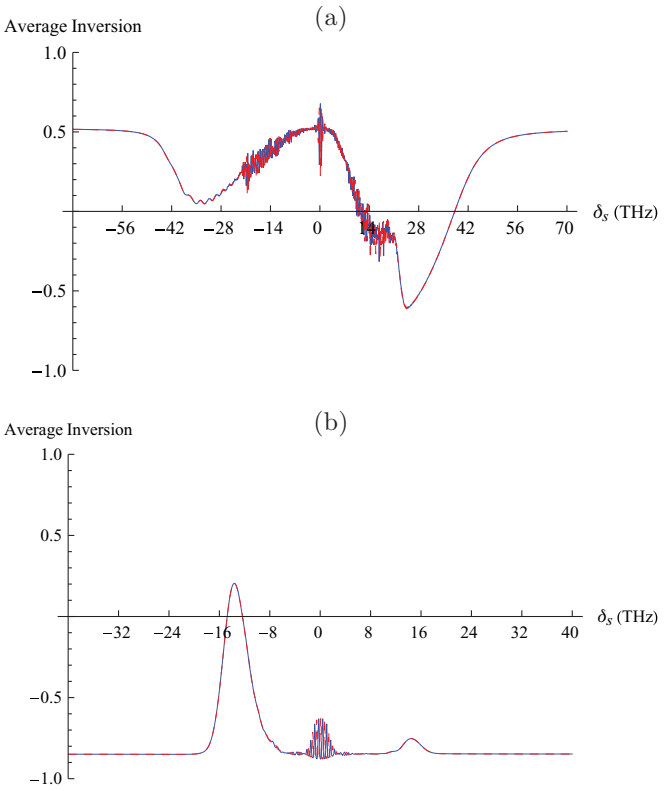

FIG. 17. (Color online) Effects of Gaussian inhomogeneous broadening on the bichromatic inversion modulation effects. The pulse duration $\tau = 5$ ps, $\gamma_{\text{high}} = 2.5$ THz, $\gamma_{\text{low}} = 5$ GHz, and $\gamma_p = 0$. The (blue) solid curves correspond to $\phi_s = 0$ and (red) dashed curves correspond to $\phi_s = \pi$. (a) Mean holding pulse detuning $\langle \Delta_{Ah} \rangle = 11$ THz with FWHM = 12 THz (1% for 1.5 μm transition frequency), $\Delta_{hE} = 4$ THz, $\epsilon_h^{\max} = 20$ THz, and $\epsilon_s^{\max} = \epsilon_h^{\max}/3$. (b) $\langle \Delta_{Ah} \rangle = -11$ THz with FWHM = 6 THz (0.5% at 1.5 μm transition frequency), $\Delta_{hE} = 15$ THz, $\epsilon_h^{\max} = 6$ THz, and $\epsilon_s^{\max} = 1.25$ THz.

when the broadening is 12 THz (about 1% for 1.5 μm transition frequency). Similarly, Fig. 20 shows the performance of logic NOT operations for 6- and 12-THz inhomogeneous broadenings. A phonon dephasing rate of $\gamma_p = 0.1$ THz is also included in these simulations. As seen from Figs. 19 and 20, even with significant(1%) inhomogeneous broadening and phonon dephasing ($\gamma_p = 0.1$ THz), the AND, OR, and NOT operations exhibit significant contrast for distinct output states of a probe signal pulse.

V. DISCUSSION

By generalizing the singly driven Bloch equation inside the structured vacuum of a photonic crystal [10,11] to a multiply driven system, we have discovered a bichromatic strong-coupling effect that enables multiwavelength channel all-optical logic on a chip. This bichromatic QD inversion modulation effect is a double-pulse extension of single-pulse dynamic switching described earlier [10,11]. The addition of a second frequency, weaker signal pulse to the previously single-pulse-driven QD leads to a remarkable strong modulation and logic-based control over the QD Bloch vector evolution path, enabling ultrafast control of QD excitations with femtojoule optical pulses in a photonic crystal chip.

As shown previously [10,11], single-pulse dynamic switching occurs through (a) field-enhanced radiative relaxation, which rapidly attracts the QD Bloch vector to parallel alignment with the pulse torque vector (steady-state attraction). This is followed by (b) coherent evolution when the pulse subsides, leaving the QD decoupled from the high LDOS of a waveguide cutoff mode (slow radiative relaxation), so that the Bloch vector adiabatically follows the pulse torque vector. The physics brought about by the second, weaker signal pulse occurs in the coherent evolution of step (b). Instead of probing the *fixed QD bare levels* such as the holding pulse, the signal pulse probes the *time-varying dressed levels* created by the holding pulse. This introduces an effective chirping between the signal field and the dressed transition resonance. For the case of a redshifted ($\Delta_{Ah} > 0$) holding pulse alone, the Bloch vector will always coherently follow the upward-pointing torque vector to the excited state. The signal pulse, however, resonantly probes the chirped dressed levels at the right Mollow sideband. When viewed from the signal pulse's own rotating frame (within the dressed-state basis created by the holding pulse), the overall torque vector

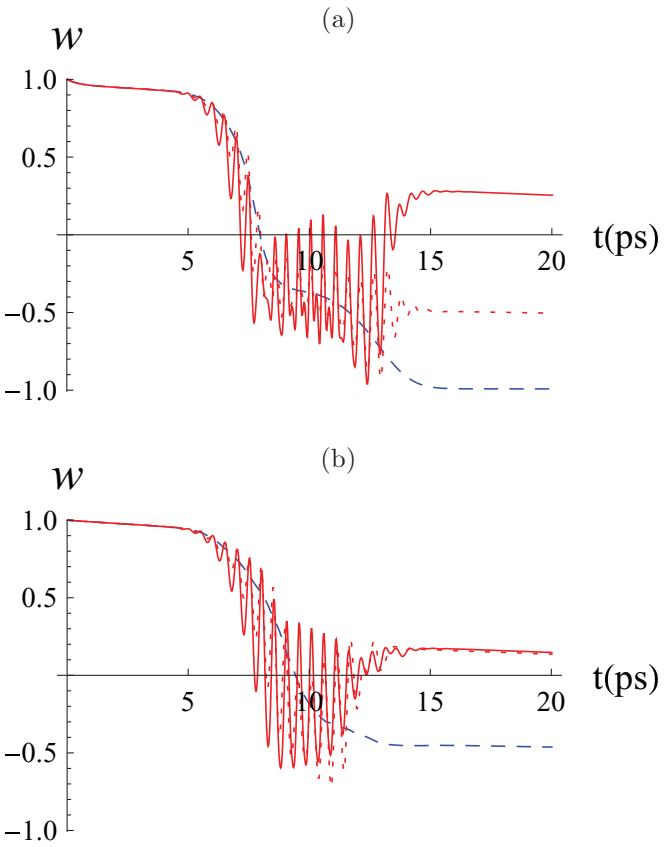

FIG. 18. (Color online) Logic operations with 6 THz (0.5% at 1.5 μm transition frequency) of inhomogeneous broadening in Q-dot transition frequency. The pulse duration $\tau = 5$ ps, $\gamma_{\text{high}} = 2.5$ THz, $\gamma_{\text{low}} = 5$ GHz, $\gamma_p = 0$, and $\delta_s = -12.5$ THz. One signal has peak Rabi frequency 1.2 THz. The (blue) dashed curves correspond to signal channel input (0,0), the (red) dotted curves correspond to input (1,0) or (0,1), and the (red) solid curves correspond to input (1,1). (a) Logic AND operation. Average $\Delta_{Ah} = -9$ THz, $\epsilon_h^{\max} = 10$ THz. (b) Logic OR operation. Average $\Delta_{Ah} = -7$ THz, $\epsilon_h^{\max} = 6$ THz.

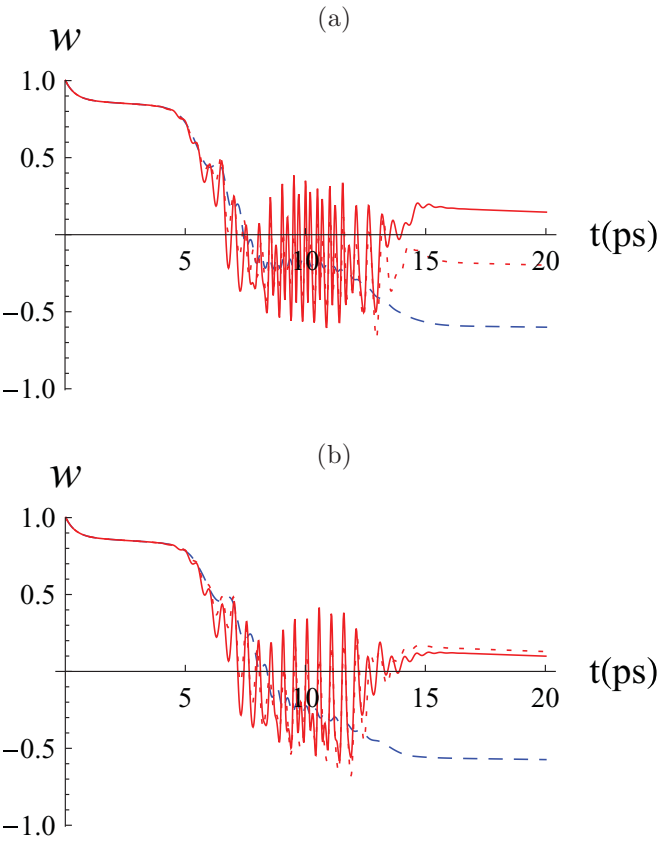

FIG. 19. (Color online) Logic operations with 12 THz (1% at 1.5 μm transition frequency) of inhomogeneous broadening in Q-dot transition frequency. The pulse duration $\tau = 5$ ps, average $\Delta_{Ah} = -6$ THz, $\delta_s = -12.5$ THz, $\gamma_{\text{high}} = 2.5$ THz, $\gamma_{\text{low}} = 5$ GHz, and $\gamma_p = 0.1$ THz. One signal has peak Rabi frequency 2.26 THz. The (blue) dashed curves correspond to signal channel input (0,0), the (red) dotted curves correspond to input (1,0) or (0,1), and the (red) solid curves correspond to input (1,1). (a) Logic AND operation, $\epsilon_h^{\max} = 12.5$ THz. (b) Logic OR operation, $\epsilon_h^{\max} = 8.2$ THz.

rotates from upward (pulse peak) to downward (pulse tail) as the detuning $\omega_h + |\mathbf{\Omega}_h| - \omega_s$ between the signal pulse and the right Mollow sideband of the holding pulse passes through zero. This chirping-induced torque vector flipping negates the population inversion that would arise by the holding pulse alone. Similarly, in the case of a signal pulse probing the chirped dressed levels of the left Mollow sideband created by a blueshifted holding pulse ($\Delta_{Ah} < 0$), the same mechanism leads to reversal of the QD final population from negative to positive.

A distinguishing characteristic of our dynamic switching and bichromatic (double-pulse) modulation of QD population inversion compared to previously studied coherent chirping-induced adiabatic inversion [30–38] is the field-enhanced radiative relaxation (step a) due to the LDOS discontinuity. This rapid steady-state attraction of the Bloch vector to the state parallel with the torque vector wipes out all memory of the initial state of the QD. Then, the coherent evolution step (b) likewise results in the same final state, independent of the system initial condition. Previously studied coherent adiabatic inversions [30–38] are lacking in this rapid, automatic prealignment of the Bloch vector. As a result, they require preparation of the QD in a particular state in advance to guarantee evolution to a desired final state. This initial-state dependence is due to the highly (Rabi) oscillatory nature of the coherent evolution when the Bloch vector is not well aligned with the torque vector. The independence of final state with respect to initial states is particularly important for applications in all-optical computing. It ensures that past logic operation history will not influence the desired outcome of the current operation.

We have demonstrated the flexibility of bichromatic QD population control for ultrafast all-optical logic gates, including AND, OR, and NOT gates. Multiwavelength channel optical logic devices of this type can be cascaded using the recently demonstrated [39] all-optical, on-chip, wavelength conversion architectures. In this case, a large number of optical logic devices can be integrated on a single photonic crystal chip for optical information processing. Input logic states are encoded into the signal-pulse stream passing through a bimodal photonic crystal waveguide simultaneously with a strong holding-pulse stream. The signal and holding pulses perform logical operations on the two-level QD medium

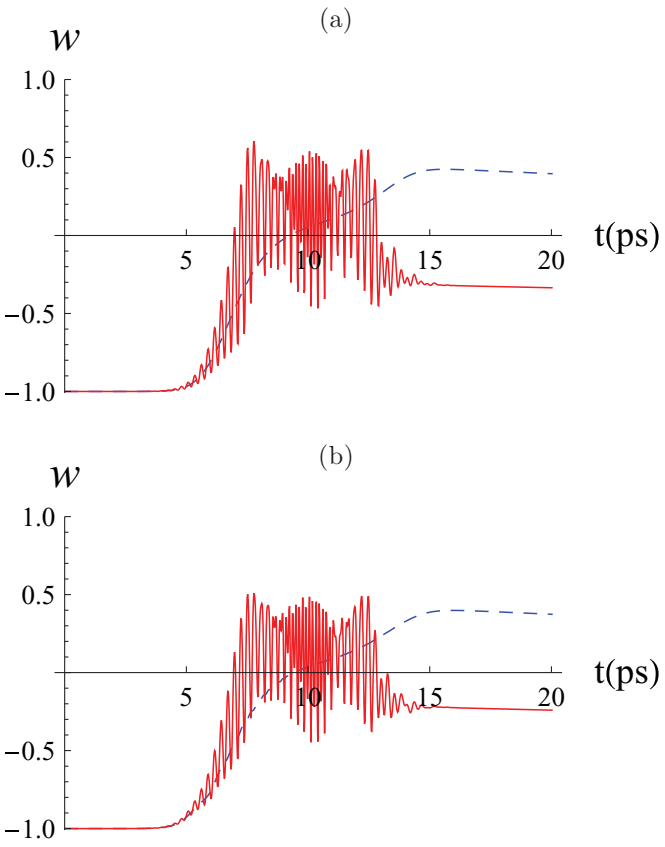

FIG. 20. (Color online) Logic NOT operations with (a) 6 THz and (b) 12 THz of inhomogeneous broadening (0.5% and 1% at 1.5 μm transition frequency, respectively) in Q-dot transition frequency. The pulse duration $\tau = 5$ ps, average $\Delta_{Ah} = 11$ THz, $\delta_s = 23$ THz, $\gamma_{\text{high}} = 2.5$ THz, $\gamma_{\text{low}} = 5$ GHz, $\gamma_p = 0.1$ THz, $\epsilon_h^{\max} = 20$ THz, and $\epsilon_s^{\max} = \epsilon_h^{\max}/3$. The (blue) dashed curves correspond to signal channel input 0, and the (red) solid curves correspond to input 1.

embedded inside the waveguide on a time scale defined by radiative relaxation in a high LDOS. The logic operation results are stored in the QDs as excited or ground states on a time scale defined by radiative relaxation in a low LDOS. They are then read out by probe pulses as optical logic outputs. Although inhomogeneous broadening and phonon dephasing tend to reduce the population contrast between distinct logic state outputs, our numerical simulations show that it is possible to reach acceptable population contrast within several picoseconds under 1% inhomogeneous broadening and 0.1-THz nonradiative dephasing rate. For successful fabrication of the photonic crystal waveguide with the desired sharp jump in LDOS, it has been shown in [26] that high-precision resolution down to several nanometers scale may be required for the active waveguide region where the QDs are embedded, while the background PBG cladding structures can accommodate substantial disorder without compromising device functionality.

Our theory assumes that each QD responds to radiation fields individually, independent of any other QDs. However, it has been shown in all-optical switching device simulation based on steady-state QD switching in PC waveguides that multiple QDs embedded in the waveguide could respond to external fields collectively if illuminated uniformly [29]. The collective responses of N_{QD} quantum dots can enhance the polarization nonlinearity and broaden the fluorescence spectrum by a factor of N_{QD} compared to the independent QD model [7,29]. If applied appropriately to the all-optical logic proposed herein, this collective effect could significantly reduce the pulse-power and field-strength requirements, and dramatically improve the response speed of the logic operations.

Our model does not consider the role of light emitted by QDs into the EM modes of the photonic crystal and how this light reacts back on the QDs together with the input laser pulses. The description of coherent feedback requires self-consistent modeling and simulation of Maxwell equations together with Bloch equations. It is shown elsewhere [40] that coherent feedback and stimulated emission in the high LDOS region effectively enhances the ratio of emission rates between the QD Mollow components in the high and low LDOS regions. Accordingly, we expect the logic operation contrasts to be further improved if we take into account these feedback effects. On the other hand, coherent feedback from QD stimulated emissions in the high LDOS region could generate memory effects that cause oscillation in QD populations and dipoles even after passage of the input pulses. This is not captured in our present simulation. In our model, no residual population oscillations are present and the QD final state after pulse passage is independent of its initial state. That is due to the rapid rate of radiative relaxation in the high LDOS region without coherent feedback. The absence of feedback is consistent with our use of a steplike LDOS profile (infinite width of high LDOS region) instead of typical LDOS spikes that arise from cavity modes.

Memory effects due to coherent feedback may be undesirable in optical logic applications involving a long sequence of optical pulses separated by short time intervals. A natural mechanism to erase the memory effects is the coupling of the quantum dots to damped phonons, causing both dephasing and nonradiative decay [40,41]. The deterioration of the QD inversion caused by this interaction could be slowed down if the dephasing and Frank-Condon effects can diminish the QD dipole that drives the population decay [40]. This balance between coherent feedback and damping caused by phonons may be important in achieving high-contrast optical logical operations without unwanted long-time memory effects. Further investigation of these issues is important in establishing practical applications of our results to on-chip all-optical information processing.

ACKNOWLEDGMENTS

This work was supported in part by the Natural Sciences and Engineering Research Council of Canada, the Ontario Premier's Platinum Fund, and the Canadian Institute for Advanced Research.

APPENDIX A: DERIVATION OF THE MASTER EQUATION FOR BICHROMATIC CONTROL OF QUANTUM DOT

In this Appendix, we derive the master equation for the reduced density operator of a quantum two-level system driven

simultaneously by a strong holding pulse and a weak signal pulse.

1. Hamiltonian in the dressed-state basis

The basis transformation (4) defines a time-dependent unitary operator B that transforms the wave function $|\psi\rangle$ and a general operator O in the bare atomic basis into the dressed atomic basis as $|\tilde{\psi}\rangle = B|\psi\rangle$ and $\tilde{O} = BOB^{\dagger}$. After this basis transformation, the Hamiltonian equation (2) becomes [42,43]

$$\tilde{H} = BHB^{\dagger} - i\hbar B\dot{B}^{\dagger} = \tilde{H}_0 + \tilde{H}_i, \tag{A1}$$

where $\tilde{H}_0 = \hbar\Omega(t)\tilde{R}_3 + \sum_\lambda \hbar\omega_\lambda a_\lambda^{\dagger}a_\lambda$ and $\tilde{H}_i = \sum_\lambda\{i\hbar g_\lambda a_\lambda^{\dagger}[-c(t)s(t)\tilde{R}_3 + c^2(t)\tilde{R}_{12} - s^2(t)\tilde{R}_{21}]+\text{H.c.}\} - i\hbar B\dot{B}^{\dagger}$. Then, by further transforming to the interaction picture via the unitary operator $U \equiv e^{i\tilde{H}_0(t-t_0)/\hbar}$, the Hamiltonian becomes

$$\tilde{H}_I = U\tilde{H}_i U^{\dagger} = \tilde{H}_{SR}^I(t) - i\hbar UB\dot{B}^{\dagger}U^{\dagger}. \tag{A2}$$

2. Derivation of the master equation

The density operator $\tilde{\chi}_I$ of the whole system and reservoir obeys the Schrödinger equation

$$\dot{\tilde{\chi}}_I(t) = \frac{1}{i\hbar}\big[\tilde{H}_I,\tilde{\chi}_I(t)\big] = \frac{1}{i\hbar}\big[\tilde{H}_{SR}^I,\tilde{\chi}_I(t)\big] - [UB\dot{B}^{\dagger}U^{\dagger},\tilde{\chi}_I(t)]. \tag{A3}$$

By substituting the formal solution of Eq. (A3) $\tilde{\chi}_I(t) = \tilde{\chi}_I(0) + (1/i\hbar)\int_0^t dt'[\tilde{H}_I(t'),\tilde{\chi}_I(t')]$ back into the first term on the right-hand side of Eq. (A3) gives

$$\dot{\tilde{\chi}}_I(t) = \frac{1}{i\hbar}\big[\tilde{H}_{SR}^I,\tilde{\chi}_I(0)\big] - [UB\dot{B}^{\dagger}U^{\dagger},\tilde{\chi}_I(t)] - \frac{1}{\hbar^2}\int_0^t dt'\big[\tilde{H}_{SR}^I(t),[\tilde{H}_I(t'),\tilde{\chi}_I(t')]\big]. \tag{A4}$$

We assume that the interaction between the atomic system and the reservoir is turned on at $t = 0$ with no correlation between the two at that moment, so that $\tilde{\chi}_I(0) = \tilde{\varrho}_I(0)R_0$. Here, $\tilde{\varrho}_I$ is the reduced density operator of the atomic system under dressed-state basis and in the interaction picture, while R_0 is the density operator of the reservoir at $t = 0$. We also assume the reservoir is in thermal equilibrium so that R_0 is diagonal. Then, we have

$$\langle a_\lambda\rangle_R = \langle a_\lambda^{\dagger}\rangle_R = 0. \tag{A5}$$

Under these assumptions, we can obtain the formal equation of motion of the reduced density operator by taking the trace over the reservoir degree of freedom in Eq. (A4):

$$\dot{\tilde{\varrho}}_I(t) = -\frac{1}{\hbar^2}\int_0^t dt'\mathrm{Tr}_R\big\{\big[\tilde{H}_{SR}^I(t),\big[\tilde{H}_{SR}^I(t'),\tilde{\chi}_I(t')\big]\big]\big\} + \frac{i}{\hbar}\int_0^t dt'\mathrm{Tr}_R\big\{\big[\tilde{H}_{SR}^I(t),[UB\dot{B}^{\dagger}U^{\dagger}(t'),\tilde{\chi}_I(t')]\big]\big\} - \mathrm{Tr}_R[UB\dot{B}^{\dagger}U^{\dagger}(t),\tilde{\chi}_I(t)], \tag{A6}$$

where, because of Eq. (A5), the following relation is used:

$$\mathrm{Tr}_R\big\{\tilde{H}_{SR}^I(t)R_0\big\} = 0. \tag{A7}$$

The standard Born approximation assumes weak coupling between the atomic system and the reservoir during the time evolution so that $\tilde{\chi}_I(t) = \tilde{\varrho}_I(t)R_0 + O(\tilde{H}_{SR}^I)$. Keeping only up to the second order in $\tilde{H}_{SR}^I$ in Eq. (A6), the radiative part of the master equation now becomes

$$\dot{\tilde{\varrho}}_I(t) = [\dot{\tilde{\varrho}}_I]_1 + [\dot{\tilde{\varrho}}_I]_2 - \mathrm{Tr}_R[UB\dot{B}^{\dagger}U^{\dagger}(t),\tilde{\chi}_I(t)] \tag{A8}$$

with the two integral terms

$$[\dot{\tilde{\varrho}}_I]_1 = -\frac{1}{\hbar^2}\int_0^t dt'\mathrm{Tr}_R\big\{\big[\tilde{H}_{SR}^I(t),\big[\tilde{H}_{SR}^I(t'),\tilde{\varrho}_I(t')R_0\big]\big]\big\}, \tag{A9a}$$

$$[\dot{\tilde{\varrho}}_I]_2 = \frac{i}{\hbar}\int_0^t dt'\mathrm{Tr}_R\big\{\big[\tilde{H}_{SR}^I(t),\big[UB\dot{B}^{\dagger}U^{\dagger}(t'),\tilde{\varrho}_I(t')R_0 + O\big(\tilde{H}_{SR}^I\big)\big]\big]\big\}. \tag{A9b}$$

As demonstrated earlier [11], in the strong field limit, the order of magnitude of the rate of variation associated with Eq. (A9b) is $O(\tau_c\dot{\theta}\gamma_-)$. Here, τ_c is the reservoir correlation time. $\dot{\theta}$ represents the angular speed of the total torque vector $\mathbf{\Omega} = \mathbf{\Omega}_h + \mathbf{\Omega}_s$, with angular speed of $\mathbf{\Omega}_h$ on the order of τ^{-1} (τ is the pulse duration) and angular speed of $\mathbf{\Omega}_s$ on the order of $\max(\tau^{-1},\delta_s)$. If $\delta_s \leqslant \tau^{-1}$ (small frequency detuning between the signal pulse and the holding pulse compared with the spectral width of the pulses), then $\dot{\theta} \approx \tau^{-1}$, so that for the same reason as shown in [11], the second integral can be ignored in the master-equation derivation. On the other hand, if $\delta_s \gg \tau^{-1}$ (large frequency detuning between signal and holding pulse), then $\dot{\theta} > \tau^{-1}$ because of the fast oscillating component at frequency δ_s. However, the contribution of this oscillatory component to $\dot{\theta}$ is averaged out over the pulse duration τ so that only the nonoscillating component determines the magnitude of $[\dot{\tilde{\varrho}}_I]_2$, which makes this second integral term also ignorable in the master equation. Consequently, the radiative part of the master equation in the dressed-state basis and interaction picture simplifies to

$$\dot{\tilde{\varrho}}_I = [\dot{\tilde{\varrho}}_I]_1 - \mathrm{Tr}_R[UB\dot{B}^{\dagger}U^{\dagger}(t),\tilde{\chi}_I(t)]. \tag{A10}$$

The first integral Eq. (A9a) can be evaluated (see Appendix B) to give

$$\begin{aligned}[\dot{\tilde{\varrho}}_I]_1 = &-\frac{\gamma_0}{2}c^2s^2(\tilde{\varrho}_I - \tilde{R}_3\tilde{\varrho}_I\tilde{R}_3) - \frac{\gamma_+}{2}c^4(\tilde{R}_{22}\tilde{\varrho}_I - \tilde{R}_{12}\tilde{\varrho}_I\tilde{R}_{21})\\ &- \frac{\gamma_-}{2}s^4(\tilde{R}_{11}\tilde{\varrho}_I - \tilde{R}_{21}\tilde{\varrho}_I\tilde{R}_{12})\\ &- \frac{cs}{2}e^{-2i\Omega t}[s^2\gamma_0(\tilde{R}_{12}\tilde{\varrho}_I - \tilde{R}_3\tilde{\varrho}_I\tilde{R}_{12})\\ &+ c^2\gamma_+(\tilde{R}_{12}\tilde{\varrho}_I + \tilde{R}_{12}\tilde{\varrho}_I\tilde{R}_3)\\ &+ s^2\gamma_-(\tilde{\varrho}_I\tilde{R}_{12} + \tilde{R}_3\tilde{\varrho}_I\tilde{R}_{12}) + c^2\gamma_0(\tilde{\varrho}_I\tilde{R}_{12} + \tilde{R}_{12}\tilde{\varrho}_I\tilde{R}_3)]\\ &- \frac{c^2s^2}{2}e^{4i\Omega t}(\gamma_- + \gamma_+)\tilde{R}_{21}\tilde{\varrho}_I\tilde{R}_{21} + \text{H.c.}\end{aligned} \tag{A11}$$

Here, γ_- is the decay rate at the left Mollow sideband $\gamma_- = 2\pi\sum_\lambda |g_\lambda|^2\delta[\omega_\lambda - \omega_h + 2\Omega(t)] \approx 2\pi\sum_\lambda |g_\lambda|^2\delta[\omega_\lambda - \omega_h + 2\Omega(t) + \nu]$ for $\nu \in [-\nu_{s^2}/2,\nu_{s^2}/2]$, while γ_0 and γ_+ are the decay rates at the central and right Mollow bands similarly defined in Appendix B. This corresponds to applying a local Markov approximation around each of the Mollow frequencies ω_h and $\omega_h \pm 2\Omega(t)$.

Finally, by transferring the radiative part of the master equation (A10) back into the Schrödinger picture and bare atomic basis (see Ref. [11] for details), and combining it with the nonradiative part of the master equation, we arrive at the master equation (6) given in the main text.

APPENDIX B: DRESSED-ATOM CORRELATIONS IN THE LOCAL MARKOV APPROXIMATION

In this Appendix, we evaluate the first integral of the master equation (A9a). The standard Markov approximation assumes that the future evolution of $\tilde{\varrho}_I(t)$ does not depend on its past values, so that $\tilde{\varrho}_I(t')$ is replaced by $\tilde{\varrho}_I(t)$ in Eq. (A9a). For convenience, we write $\tilde{H}^I_{SR} = \sum_{i=1}^{6} \tilde{S}_i \tilde{\Gamma}_i$, where

$$\begin{aligned} \tilde{S}_1 = \tilde{S}_4 = \tilde{R}_3, \quad \tilde{S}_2 = \tilde{S}_5 = \tilde{R}_{12}, \quad \tilde{S}_3 = \tilde{S}_6 = \tilde{R}_{21}, \\ \tilde{\Gamma}_1 = \tilde{\Gamma}_4^\dagger = -i\hbar \sum_\lambda g_\lambda a_\lambda^\dagger c(t) s(t) e^{i\Delta_\lambda t}, \\ \tilde{\Gamma}_2 = \tilde{\Gamma}_5^\dagger = i\hbar \sum_\lambda g_\lambda a_\lambda^\dagger c^2(t) e^{i[\Delta_\lambda - 2\Omega(t)]t}, \\ \tilde{\Gamma}_3 = \tilde{\Gamma}_6^\dagger = -i\hbar \sum_\lambda g_\lambda a_\lambda^\dagger s^2(t) e^{i[\Delta_\lambda + 2\Omega(t)]t}. \end{aligned} \tag{B1}$$

Now, by invoking the Born-Markov approximation, the first integral (A9a) becomes

$$\begin{aligned} [\dot{\tilde{\varrho}}_I]_1 = -\sum_{i,j} \frac{1}{\hbar^2} \int_0^t dt' \{ [\tilde{S}_i \tilde{S}_j \tilde{\varrho}_I(t) \\ - \tilde{S}_j \tilde{\varrho}_I(t) \tilde{S}_i] \langle \tilde{\Gamma}_i(t) \tilde{\Gamma}_j(t') \rangle_R \\ + [\tilde{\varrho}_I(t) \tilde{S}_j \tilde{S}_i - \tilde{S}_i \tilde{\varrho}_I(t) \tilde{S}_j] \langle \tilde{\Gamma}_j(t') \tilde{\Gamma}_i(t) \rangle_R \}, \end{aligned} \tag{B2}$$

where $\langle \tilde{\Gamma}_i(t) \tilde{\Gamma}_j(t') \rangle_R = \mathrm{Tr}_R[R_0 \tilde{\Gamma}_i(t) \tilde{\Gamma}_j(t')]$, $\tilde{\varrho}_I(t)$ is the reduced density operator of the atom, and R_0 is the reservoir part of the density operator.

If we make the substitution $t' = t - \tau$ and assume the electromagnetic reservoir to be unoccupied, then Eq. (B2) can be simplified to

$$\begin{aligned} [\dot{\tilde{\varrho}}_I]_1 = -\frac{1}{\hbar^2} \sum_{\substack{j=1,2,3 \\ i=4,5,6}} [\tilde{S}_i \tilde{S}_j \tilde{\varrho}_I(t) - \tilde{S}_j \tilde{\varrho}_I(t) \tilde{S}_i] \\ \times \int_0^t d\tau \langle \tilde{\Gamma}_i(t) \tilde{\Gamma}_j(t-\tau) \rangle_R \\ - \frac{1}{\hbar^2} \sum_{\substack{j=4,5,6 \\ i=1,2,3}} [\tilde{\varrho}_I(t) \tilde{S}_j \tilde{S}_i - \tilde{S}_i \tilde{\varrho}_I(t) \tilde{S}_j] \\ \times \int_0^t d\tau \langle \tilde{\Gamma}_j(t-\tau) \tilde{\Gamma}_i(t) \rangle_R. \end{aligned} \tag{B3}$$

To facilitate the evaluation of the correlation integrals, we spectrally expand the time-dependent factors $f(t) \equiv c(t)s(t)$, $c^2(t)$, and $s^2(t)$ in $\tilde{\Gamma}_i$ as follows:

$$f(t) = \frac{1}{\sqrt{2\pi}} \int_{-\infty}^{\infty} f_\nu e^{i\nu t} d\nu \approx \frac{1}{\sqrt{2\pi}} \int_{-\frac{\nu_f}{2}}^{\frac{\nu_f}{2}} f_\nu e^{i\nu t} d\nu. \tag{B4}$$

We assume above that the main spectral widths of the functions $cs(t)$, $c^2(t)$, and $s^2(t)$ are ν_{cs}, ν_{c^2}, and ν_{s^2}, respectively.

Now we evaluate the integrals of each term contained in Eq. (B3) for different values of i and j. For $i = 4$, $j = 1$,

$$\begin{aligned} \int_0^t d\tau \langle \tilde{\Gamma}_4(t) \tilde{\Gamma}_1(t-\tau) \rangle_R \\ = \hbar^2 c(t) s(t) \sum_\lambda |g_\lambda|^2 \int_0^t d\tau \, c(t-\tau) s(t-\tau) e^{-i\Delta_\lambda \tau}. \end{aligned} \tag{B5}$$

The upper limit t of the τ integral in Eq. (B5) is on the typical time scale for significant changes in the density operator. In the Markov approximation, t is much larger than the decay time scale of reservoir correlations that governs the τ integral. As a result, we can approximate the τ integral by extending its upper limit to ∞ [44]. This integral can then be evaluated through the following relation [44,45]:

$$\lim_{t\to\infty} \int_0^t d\tau \, e^{-i\omega\tau} = \pi\delta(\omega) - iP\left(\frac{1}{\omega}\right), \tag{B6}$$

where P indicates the Cauchy principal value. The first delta function term is real, which leads to a decay term of the master equation. The second principal value term is complex, which gives rise to an oscillatory term in the master equation that acts as shift in the atomic transition frequency [44]. This frequency shift can always be accounted into the transition frequency, and we can only focus on the decay dynamics. Consequently, by discarding the principal value term and using (B4), we get

$$\begin{aligned} \int_0^t d\tau \langle \tilde{\Gamma}_4(t) \tilde{\Gamma}_1(t-\tau) \rangle_R \\ = \frac{\hbar^2}{2} c(t) s(t) \frac{1}{\sqrt{2\pi}} \int_{-\frac{\nu_{cs}}{2}}^{\frac{\nu_{cs}}{2}} d\nu (cs)_\nu e^{i\nu t} \gamma_{\omega_h - \nu}, \end{aligned} \tag{B7}$$

where $\gamma_{\omega_h-\nu} = 2\pi \sum_\lambda |g_\lambda|^2 \delta(\omega_\lambda - [\omega_h - \nu])$ and $(cs)_\nu$ is defined in Eq. (B4). The spectral width ν_{cs} of cs is of order $\max(\tau^{-1}, \delta_s)$. When $\delta_s \leqslant \tau^{-1}$, the spectral width $\nu_{cs} \sim \tau^{-1}$ is confined by the spectral width of the pulse. We also assume that the photonic density of states is smooth in the region $[\omega_h - \nu_{cs}/2, \omega_h + \nu_{cs}/2]$ such that $\gamma_{\omega_h-\nu} \approx \gamma_{\omega_h} \equiv \gamma_0$ for $-\nu_{cs}/2 \leqslant \nu \leqslant \nu_{cs}/2$. On the other hand, if $\delta_s \gg \tau^{-1}$, there would be major spectral components $(cs)_\nu$ at $\nu \approx \pm\delta_s$ far away from the central frequency ω_h in the integral (B7). In this relatively large frequency region $[\omega_h - \nu_{cs}/2, \omega_h + \nu_{cs}/2]$, a smooth decay rate $\gamma_{\omega_h-\nu}$ is not satisfied. However, for these high-frequency components, the corresponding fast oscillating factor $e^{i\nu t}$ renders their average contribution to the system evolution over a time scale of τ to be vanishingly small regardless of the value of $\gamma_{\omega_h-\nu}$. In this case, we can also replace $\gamma_{\omega_h-\nu}$ with γ_0 without causing any material difference. This analysis implies that for fast oscillating dressed states (due to large detuning between the holding and signal pulse), only the nonoscillating components of the dressed-state coefficients c and s are important in determining the radiative decay rates of the dressed system. Then, by using the inverse of Eq. (B4) in (B7), we arrive at

$$\int_0^t d\tau \langle \tilde{\Gamma}_4(t) \tilde{\Gamma}_1(t-\tau) \rangle_R \approx \frac{\hbar^2}{2} c^2(t) s^2(t) \gamma_0. \tag{B8}$$

Effectively, we have made a "local Markov" approximation around the central Mollow band located at ω_h. As long as the

central Mollow band is far enough from the band edge (such that the edge ω_E is outside the spectral width ν_{cs} around the central Mollow band), or that the spectral components $(cs)_\nu$ that move into the band edge have enough detuning from the central component at ω_h, the approximation (B8) is reasonable.

For $i = 5$, $j = 2$,

$$\int_0^t d\tau \langle \tilde{\Gamma}_5(t)\tilde{\Gamma}_2(t-\tau)\rangle_R = \hbar^2 c^2(t) \sum_\lambda |g_\lambda|^2, \int_0^t d\tau\, c^2(t-\tau) e^{-i[\Delta_\lambda - 2\Omega(t)]t} \times e^{i[\Delta_\lambda - 2\Omega(t-\tau)](t-\tau)}. \tag{B9}$$

Under Markov approximation, we replace $\Omega(t-\tau)$ with $\Omega(t)$ in the τ integration. Then, by using Eq. (B4), we obtain

$$\int_0^t d\tau \langle \tilde{\Gamma}_5(t)\tilde{\Gamma}_2(t-\tau)\rangle_R \approx \hbar^2 c(t)^2 \int_{-\frac{\nu_{c^2}}{2}}^{\frac{\nu_{c^2}}{2}} d\nu\, c_\nu^2 e^{i\nu t} \sum_\lambda |g_\lambda|^2 \times \int_0^t d\tau\, e^{-i\nu\tau - i[\Delta_\lambda - 2\Omega(t)]\tau}. \tag{B10}$$

Similar to the evaluation of Eq. (B5), by extending the upper limit of the τ integral to infinity (because in the Markov approximation, the contribution of the τ integral mainly comes from the reservoir correlation decay time scale that is much shorter than the density operator evolution time scale t in the upper limit), and making use of Eq. (B6), we obtain

$$\int_0^t d\tau \langle \tilde{\Gamma}_5(t)\tilde{\Gamma}_2(t-\tau)\rangle_R \approx \frac{\hbar^2}{2} c^2(t) \int_{-\frac{\nu_{c^2}}{2}}^{\frac{\nu_{c^2}}{2}} d\nu\, c_\nu^2 e^{i\nu t} 2\pi \times \sum_\lambda |g_\lambda|^2 \delta[\omega_\lambda - \omega_h - 2\Omega(t) + \nu] \approx \frac{\hbar^2}{2} c^4(t)\gamma_+, \tag{B11}$$

where $\gamma_+ = 2\pi \sum_\lambda |g_\lambda|^2 \delta(\omega_\lambda - \omega_h - 2\Omega(t)) \approx 2\pi \sum_\lambda |g_\lambda|^2 \delta(\omega_\lambda - \omega_h - 2\Omega(t) + \nu)$ for $\nu \in [-\nu_{c^2}/2, \nu_{c^2}/2]$. This corresponds to a local Markov approximation around the right Mollow sideband located at $\omega_h + 2\Omega(t)$.

Following the same steps for other combinations of i, j in Eq. (B3), we obtain the first integral of the radiative master equation given in Eq. (A11).

[1] S. John, Phys. Rev. Lett. **53**, 2169 (1984).
[2] S. John, Phys. Rev. Lett. **58**, 2486 (1987).
[3] V. P. Bykov, Sov. J. Quantum Electron. **4**, 861 (1975) [Kvantovaia Elektronika (Moscow), **1**, 1557 (1974)].
[4] E. Yablonovitch, Phys. Rev. Lett. **58**, 2059 (1987).
[5] S. John and J. Wang, Phys. Rev. Lett. **64**, 2418 (1990).
[6] S. John and T. Quang, Phys. Rev. Lett. **74**, 3419 (1995).
[7] M. Florescu and S. John, Phys. Rev. A **69**, 053810 (2004).
[8] M. Florescu and S. John, Phys. Rev. A **64**, 033801 (2001).
[9] S. John and M. Florescu, J. Opt. A: Pure Appl. Opt. **3**, S103 (2001).
[10] X. Ma and S. John, Phys. Rev. Lett. **103**, 233601 (2009).
[11] X. Ma and S. John, Phys. Rev. A **80**, 063810 (2009).
[12] A. Chutinan, S. John, and O. Toader, Phys. Rev. Lett. **90**, 123901 (2003).
[13] A. Chutinan and S. John, Phys. Rev. E **71**, 026605 (2005).
[14] A. Chutinan and S. John, Phys. Rev. B **72**, 161316 (2005).
[15] A. Chutinan and S. John, Opt. Express **14**, 1266 (2006).
[16] T. Y. M. Chan and S. John, Phys. Rev. A **78**, 033812 (2008).
[17] J. Lourtioz, H. Benisty, V. Berger, J. Gerard, D. Maystre, and A. Tchelnokov, *Photonic Crystals* (Springer, New York, 1999).
[18] T. Yoshie, A. Scherer, J. Hendrickson, G. Khitrova, H. M. Gibbs, G. Rupper, C. Ell, O. B. Shchekin, and D. G. Deppe, Nature (London) **432**, 200 (2004).
[19] H. Benisty, J. Lourtioz, A. Chelnokov, S. Combrie, and X. Checoury, Proc. IEEE **94**, 997 (2006).
[20] J. P. Reithmaier, G. Sek, A. Loffler, C. Hofmann, S. Kuhn, S. Reitzenstein, L. V. Keldysh, V. D. Kulakovskii, T. L. Reinecke, and A. Forchel, Nature (London) **432**, 197 (2004).
[21] E. Peter, P. Senellart, D. Martrou, A. Lemaitre, J. Hours, J. M. Gerard, and J. Bloch, Phys. Rev. Lett. **95**, 067401 (2005).
[22] X. Xu, B. Sun, P. R. Berman, D. G. Steel, A. S. Bracker, D. Gammon, and L. J. Sham, Science **317**, 929 (2007).
[23] A. N. Vamivakas, Y. Zhao, C. Lu, and M. Atature, Nat. Phys. **5**, 198 (2009).
[24] E. B. Flagg, A. Muller, J. W. Robertson, S. Founta, D. G. Deppe, M. Xiao, W. Ma, G. J. Salamo, and C. K. Shih, Nat. Phys. **5**, 203 (2009).
[25] R. Wang and S. John, Phys. Rev. A **70**, 043805 (2004).
[26] S. John and R. Wang, Photonics Nanostruct.: Fund. Applicat. **2**, 137 (2004).
[27] Z. Ficek and H. S. Freedhoff, Phys. Rev. A **53**, 4275 (1996).
[28] X. Ma and S. John (unpublished).
[29] D. Vujic and S. John, Phys. Rev. A **76**, 063814 (2007).
[30] E. B. Treacy, Phys. Lett. A **27A**, 421 (1968).
[31] M. M. T. Loy, Phys. Rev. Lett. **32**, 814 (1974).
[32] L. Allen and J. H. Eberly, *Optical Resonance and Two-Level Atoms* (Wiley, New York, 1975).
[33] S. M. Hamadani, A. T. Mattick, N. A. Kurnit, and A. Javan, Appl. Phys. Lett. **27**, 21 (1975).
[34] B. Broers, H. B. van Linden van den Heuvell, and L. D. Noordam, Phys. Rev. Lett. **69**, 2062 (1992).
[35] M. E. Crenshaw, M. Scalora, and C. M. Bowden, Phys. Rev. Lett. **68**, 911 (1992).
[36] M. E. Crenshaw and C. M. Bowden, Phys. Rev. Lett. **69**, 3475 (1992).
[37] D. Goswami and W. S. Warren, Phys. Rev. A **50**, 5190 (1994).
[38] N. V. Vitanov, T. Halfmann, B. W. Shore, and K. Bergmann, Annu. Rev. Phys. Chem. **52**, 763 (2001).
[39] D. Vujic and S. John, Phys. Rev. A **79**, 053836 (2009).
[40] H. Takeda and S. John, Phys. Rev. A (to be published).
[41] C. Roy and S. John, Phys. Rev. A **81**, 023817 (2010).
[42] A. Mostafazadeh, *Dynamical Invariants, Adiabatic Approximation, and the Geometric Phase* (Nova Science Publishers, Huntington, NY, 2001).
[43] A. Mostafazadeh, Phys. Lett. A **320**, 375 (2004).
[44] H. Carmichael, *An Open Systems Approach to Quantum Optics* (Springer-Verlag, New York, 1993).
[45] R. R. Puri, *Mathematical Methods of Quantum Optics*, 1st ed. (Springer, New York, 2001).